

XMM-NEWTON OBSERVATIONS OF LUMINOUS SOURCES IN NEARBY GALAXIES NGC 4395, NGC 4736, AND NGC 4258

A. AKYUZ¹, S. KAYACI², H. AVDAN¹, M. E. OZEL³, E. SONBAS⁴, AND S. BALMAN⁵

¹ Department of Physics, University of Cukurova, 01330 Adana, Turkey; aakyuz@cu.edu.tr

² Department of Astronomy, University of Erciyes, Kayseri, Turkey

³ Faculty of Arts and Sciences, Çağ University, 33800 Yenice, Tarsus, Mersin, Turkey

⁴ Department of Physics, University of Adıyaman, 02040 Adıyaman, Turkey

⁵ Department of Physics, Middle East Technical University, 06531 Ankara, Turkey

Received 2012 August 2; accepted 2012 December 21; published 2013 February 5

ABSTRACT

We present the results of a study of non-nuclear discrete sources in a sample of three nearby spiral galaxies (NGC 4395, NGC 4736, and NGC 4258) based on *XMM-Newton* archival data supplemented with *Chandra* data for spectral and timing analyses. A total of 75 X-ray sources have been detected within the D_{25} regions of the target galaxies. The large collecting area of *XMM-Newton* makes the statistics sufficient to obtain spectral fitting for 16 (about 20%) of these sources. Compiling the extensive archival exposures available, we were able to obtain the detailed spectral shapes of diverse classes of point sources. We have also studied temporal properties of these luminous sources. Eleven of them are found to show short-term (less than 80 ks) variation while eight of them show long-term variation within factors of ~ 2 – 5 during a time interval of ~ 2 – 12 years. Timing analysis provides strong evidence that most of these sources are accreting X-ray binary systems. One source that has properties different from others was suspected to be a supernova remnant, and our follow-up optical observation confirmed this. Our results indicate that sources within the three nearby galaxies are showing a variety of source populations, including several ultraluminous X-ray sources, X-ray binaries, transients together with a super soft source, and a background active galactic nucleus candidate.

Key words: galaxies: individual (NGC 4736, NGC 4395, NGC 4258) – X-rays: binaries – X-rays: galaxies

Online-only material: color figures

1. INTRODUCTION

The increased imaging and energy resolution capabilities of the new generation X-ray observatories such as *XMM-Newton* and *Chandra* provide a better understanding of the X-ray emission from nearby galaxies. A combination of a number of discrete sources, hot interstellar gas, and a probable active galactic nucleus (AGN) are thought to produce the observed X-ray emission from such galaxies (Fabbiano 1989). A large number of discrete sources have already been detected by *XMM-Newton* and *Chandra* in the disks of nearby galaxies such as M 31 (Pietsch 2005; Kong et al. 2002, 2003), M 33 (Pietsch 2004; Plucinsky et al. 2008) M 81 (Swartz et al. 2003), and M 101 (Pence et al. 2001; Jenkins et al. 2004). These sources are typically high- and low-mass X-ray binaries (XRBs), supernova remnants (SNRs), bright super soft sources (SSS), and a number of very luminous sources, the so-called ultraluminous X-ray sources (ULXs).

To study the discrete X-ray source population in nearby spiral galaxies, a sample of three (NGC 4395, NGC 4736, and NGC 4258) was chosen for this work. All three have a low-activity Seyfert nucleus. Their low foreground absorption $(1.20\text{--}1.43) \times 10^{20} \text{ cm}^{-2}$ (Dickey & Lockman 1990) also made them good targets for exploring such discrete X-ray sources.

NGC 4395 is classified as one of the nearest and least luminous ($L_{\text{Bol}} \sim 5 \times 10^{40} \text{ erg s}^{-1}$) type 1 Seyfert galaxies (Filippenko & Sargent 1989). This dwarf galaxy appears to harbor a central black hole, likely to be in the $\sim 10^4\text{--}10^5 M_{\odot}$ range, significantly lower than more luminous Seyferts with black hole masses typically in the range $\sim 10^6\text{--}10^8 M_{\odot}$ (Vaughan et al. 2005). Its nucleus has been the subject of several X-ray studies

since the *ROSAT* observations (Moran et al. 1999; Lira et al. 1999), which reported that its nuclear X-ray source displays a large amplitude variability on short timescales and has a soft X-ray spectrum. Also, five X-ray sources, one being significantly brighter than the nucleus, were detected within $\sim 3'$ of its nucleus. Later, observations by *Chandra* and *XMM-Newton* confirmed the variable nature of its active nucleus (Moran et al. 2005; Vaughan et al. 2005).

Our next target, NGC 4736 (M94), is classified as a low-luminosity galaxy with the closest sample of a low-ionization nuclear emission-line region (LINER) nucleus (Filippenko & Sargent 1985). Two bright sources were detected by *ROSAT* observations in its nuclear area (Cui et al. 1997). One of them was consistent with the nucleus of the galaxy and almost one-third of the total observed flux of (0.1–2) keV was caused by the emission from the compact source in the center with an extended distribution of hot gas. Twelve discrete sources (including the galactic nucleus itself) were identified by *ROSAT/HRI* data in its optical disk and ring regions (Roberts et al. 1999). The galaxy was also observed with *BeppoSAX* in the 0.1–100 keV band and with *Chandra/ACIS-S* for a high-resolution study of its nuclear region (Pellegrini et al. 2002). Those observations concluded that the LINER activity was due to a low-luminosity AGN at the center. Eracleous et al. (2002) had already examined the high concentration of luminous sources in the nucleus of NGC 4736 by *Chandra*. They suggested that the galaxy was in a recent starburst phase where the emission was dominated by dense clusters of XRBs.

Our third target, NGC 4258 (M106) is a bright nearby type 1.9 Seyfert galaxy. It is also known by its anomalous arms discovered by $H\alpha$ imaging (Courtes et al. 1993). Water

Table 1
General Properties of the Sample Galaxies Studied in Our Work

Galaxy	R.A., Decl. (J2000)	Hubble Type ^a	Distance ^b (Mpc)	Inclination (deg)	n_H^c (10^{20} cm^{-2})	$D_{25\text{corr}}^d$ (arcmin)
NGC 4395	12:25:48.9 +33:32:47.8	SA(s)m	4.2	38	1.33	13.3
NGC 4736	12:50:52.6 +41:07:09.3	(R)SA(r)ab	4.3	33	1.43	11.8
NGC 4258	12:18:57.6 +47:18:13.4	SAB(s)bc	7.7	71	1.20	14.2

Notes.^a Winter et al. (2006).^b Swartz et al. (2004) and Winter et al. (2006).^c Column density, obtained from the Web version of the n_H FTOOL.^d D_{25} diameter; defined by the 25 mag arcsec⁻² brightness level.

Table 2
Locations of Luminous Sources (as Defined in the Text) with Respect to the Galaxy Centers
and Cross Identifications for the Sources in the Three Galaxies Studied

Galaxy	Source	Separation (arcmin)	<i>ROSAT</i> ID	<i>Chandra</i> ID
NGC 4395	XMM-2	2.9	P1 ^a	
	XMM-5	2.1	P2 ^a	CXOU J122539.5+333204 ^d
	XMM-6	0.7	P3 ^a	CXOU J122549.063+333201.82 ^e
	XMM-10	2.0	P4 ^a	CXOU J122547.287+333447.75 ^e
	XMM-23	1.9		CXOU J122545.271+333103.40 ^e
NGC 4736	XMM-2	0.9		CXOU J125048.598+410742.49 ^e
	XMM-12	2.3	X-7 ^b	CXOU J125047.618+410512.26 ^e
	XMM-18	2.1	X-13 ^b	CXOU J125104.4+410725 ^f
NGC 4258	XMM-2	3.1		
	XMM-3	2.1	P16 ^c	CXOU J121857.8+471607 ^d
	XMM-6	2.4		CXOU J121843.8+471731 ^d
	XMM-8	1.5	P14 ^c	
	XMM-10	6.4	P13 ^c	
	XMM-16	3.3		CXOU J121839.317+471919.27 ^e
	XMM-17	2.0		CXOU J121849.481+471646.42 ^e
	XMM-21	3.2	P15 ^c	CXOU J121856.419+472125.56 ^e

Notes.^a The 2RXP Catalog 2000.^b Roberts et al. (1999).^c Pietsch et al. (1994).^d Swartz et al. (2004).^e Liu 2011.^f From the present work.

maser line emission of rotating gas near its center indicated a mass of $3.6 \times 10^7 M_\odot$ in a disk of radius ranging from 0.12 to 0.25 pc (Miyoshi et al. 1995). *ROSAT* observations of NGC 4258 resolved the anomalous spiral arms forming the boundary of diffuse emission. Fifteen X-ray point sources associated with the galaxy were identified by *ROSAT* observations (Pietsch et al. 1994; Cecil et al. 1995; Vogler & Pietsch 1999). These observations could not detect the Seyfert nucleus of the galaxy as a point source. The first detection of active nucleus was reported by *ASCA* observations. It was modeled by an absorbed power-law spectrum with a photon index $\Gamma \sim 1.8$. The unabsorbed 2–10 keV luminosity of the source was $L_X = 4 \times 10^{40} \text{ erg s}^{-1}$ obscured by a column density of $N_H \sim 1.5 \times 10^{23} \text{ cm}^{-2}$. An Fe K α emission line was detected with an equivalent width $0.25 \pm 0.10 \text{ keV}$ (Makishima et al. 1994).

NGC 4258 was also observed by *XMM-Newton*, which showed a hard nuclear point source that could be modeled by a highly absorbed power-law spectrum with no narrow Fe K α emission (Pietsch & Read 2002). A series of observations were also made by *Chandra* to study its various properties (Young & Wilson 2004). These observations examined the spectrum of

the low-luminosity AGN, which was well described by a hard X-ray power law and a variable luminosity with a constant thermal soft X-ray component. They also discussed the first detection of extragalactic Fe absorption line at 6.9 keV, with a very inclined accretion disk varying on a timescale of 6 ks. Yang et al. (2007) studied *Chandra* and *XMM-Newton* spectra for anomalous arms and active jets. They confirmed that the X-ray emission from these arms has a thermal nature, suggesting that currently active jets could be responsible for heating the gas in the arms.

In the present work, we will investigate the spectral and timing properties of the bright point-like non-nuclear sources in these three galaxies, first as observed by *XMM-Newton* with a more extended database compared to the previous studies and later by *Chandra* to supplement their spectral and timing properties. General properties of the galaxies are listed in Table 1. We will restrict ourselves to the off-nucleus luminous sources with a sufficient signal-to-noise ratio (S/N) to perform spectral fitting. Source locations with respect to the galaxy centers and their cross identifications (if any) have been listed in Table 2.

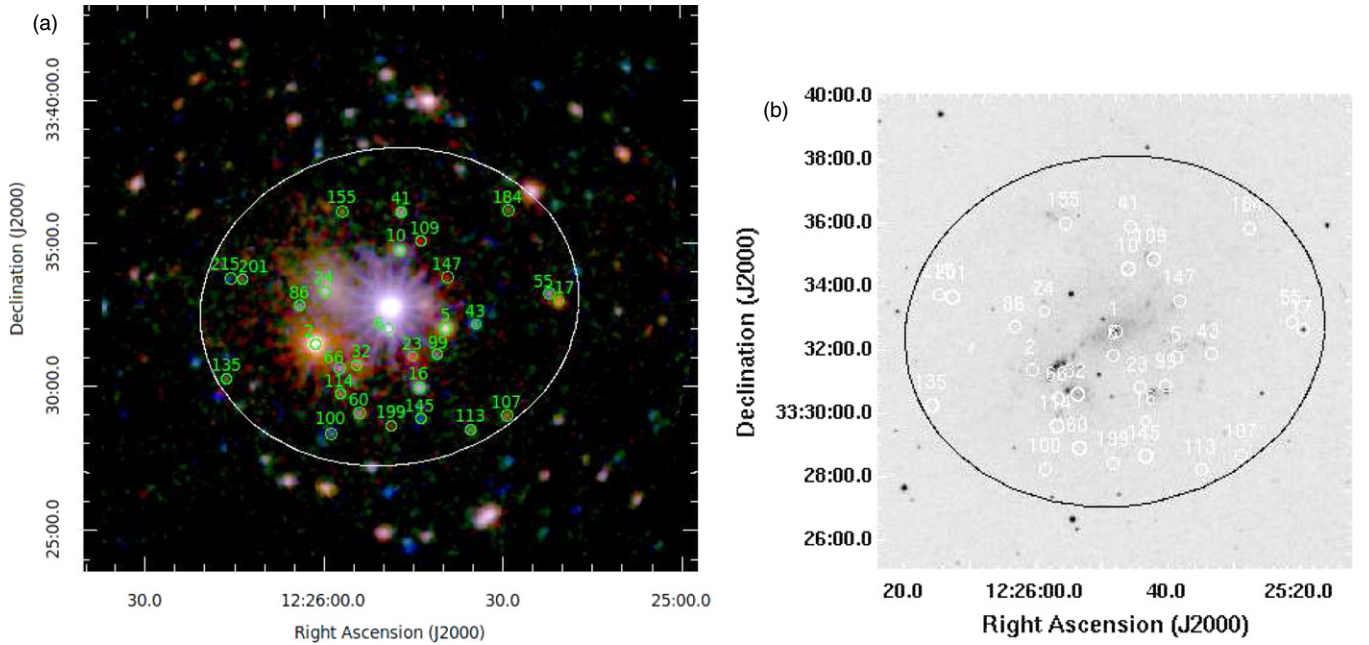


Figure 1. (a) *XMM-Newton* RGB image of NGC 4395. Red—(0.2–1) keV, green—(1–2) keV, and blue—(2–12) keV. The D_{25} ellipse is also shown for comparison. (b) *XMM-Newton* source positions are overlaid on a DSS1 optical blue image (circles are not representing positional error radii). The detected point sources inside the D_{25} ellipse are specified as off-nuclear galactic objects.

(A color version of this figure is available in the online journal.)

The paper is organized as follows. In Section 2, we outline the data reduction and source selection criteria. In Section 3, the spectral fitting and timing analysis techniques are described; and in Section 4, a detailed discussion of spectral and temporal results for individual sources in the galaxies is presented. The overall properties of their X-ray emission are discussed in Section 5.

2. OBSERVATIONS AND DATA REDUCTION

2.1. *XMM-Newton* Observations

The data used for the analysis were retrieved from the *XMM-Newton* public archive. The *XMM-Newton* satellite (Jansen et al. 2001) has three EPIC cameras at its focal plane: one uses a pn-CCD (Strüder et al. 2001) and the other two are MOS-CCD detectors (Turner et al. 2001). Instruments were operated in the full-frame imaging mode and used thin or medium filters for pn and MOS. We analyzed the pipeline-processed data by using the standard software tools of the *XMM-Newton* Science Analysis System (XMM-SAS) v 10.0 (Gabriel et al. 2004). In SAS, X-ray events corresponding to $\text{PATTERN} \leq 4$ (singles and doubles) were then selected with the $\text{FLAG}==0$ option for the pn camera, and $\text{PATTERN} \leq 12$ events were used for the MOS cameras. Source detection was performed using the standard maximum likelihood technique as implemented by the SAS tool *edetect_chain*. Each source inside the D_{25} ellipse was checked to exclude false or doubtful sources, according to the automatic selection procedure in SAS. The log of observations, including the dates, IDs, exposure times, and the type of EPIC camera for each target, are given in Table 3.

In the analysis, we simultaneously used data from EPIC-pn and EPIC MOS for each galaxy to determine the spectra of the sources (with the exception of the MOS data for NGC 4395, which has poor statistics). Note also that EPIC-pn has more source counts due to its better sensitivity when compared to the MOS detectors. Figures 1(a), 2(a), and 3(a) show the combined

Table 3
The Log of *XMM-Newton* Observations for the Three Galaxies Studied

Galaxy	ObsId	Obs. Date	Exposure ^a (s)	Mode ^b /Filter
NGC 4395	0112521901	2002.05.31	13978	FF/thin
	0142830101	2003.11.30	89000	FF/medium
NGC 4736	0094360701	2002.06.26	17046	FF/medium
	0404980101	2006.11.27	37245	FF/thin
NGC 4258	0110920101	2000.12.08	16548	FF/medium
	0059140101	2001.05.06	9488	FF/medium
	0059140201	2001.06.17	10058	FF/medium
	0059140401	2001.12.17	11798	FF/medium
	0059140901	2002.05.22	13646	FF/medium
	0400560301	2006.11.17	62635	FF/medium

Notes.

* We used only the observations highlighted in bold for the spectral analysis.

^a A net good time for EPIC-pn after most prominent flares were cut.

^b FF: full frame.

exposure-corrected EPIC-pn, MOS1, and MOS2 true color images of the presently analyzed archival data for the sample galaxies. Inclination-corrected D_{25} ellipses are also shown for comparison and identification. The detected point sources inside a D_{25} ellipse were specified as off-nuclear objects. We numbered them as XMM-n, n representing the source number with a decreasing pn count rate. Figures 1(b), 2(b), and 3(b) show *XMM-Newton* point source positions overlaid on a DSS1 optical blue image of each galaxy. The detected X-ray source parameters in each galaxy are summarized in Tables 4, 5, and 6, respectively. In each table the source ID (Column 1), its position (Columns 2 and 3), the likelihood of existence (where a likelihood value of 10 corresponds to a detection probability above 4σ ; Column 4), integrated (pn + MOS1 + MOS2) count rates with

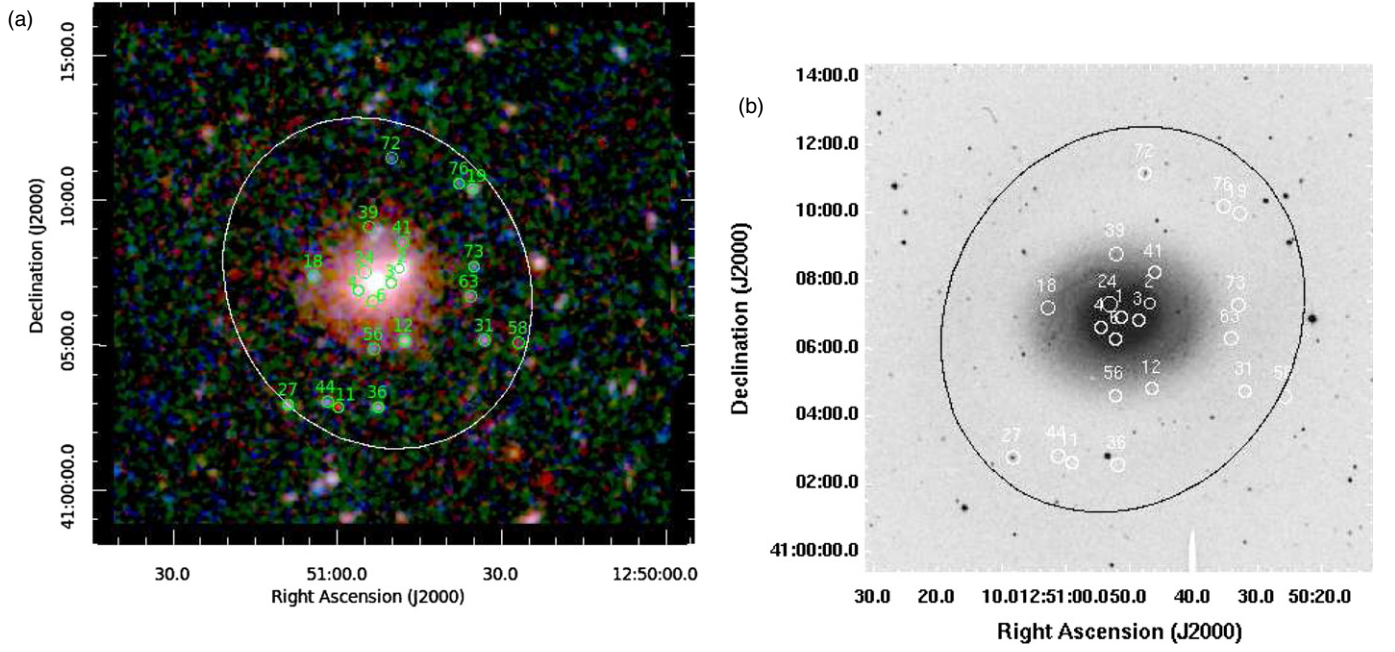


Figure 2. *XMM-Newton* RGB image of NGC 4736. Definitions are the same as in Figure 1.
(A color version of this figure is available in the online journal.)

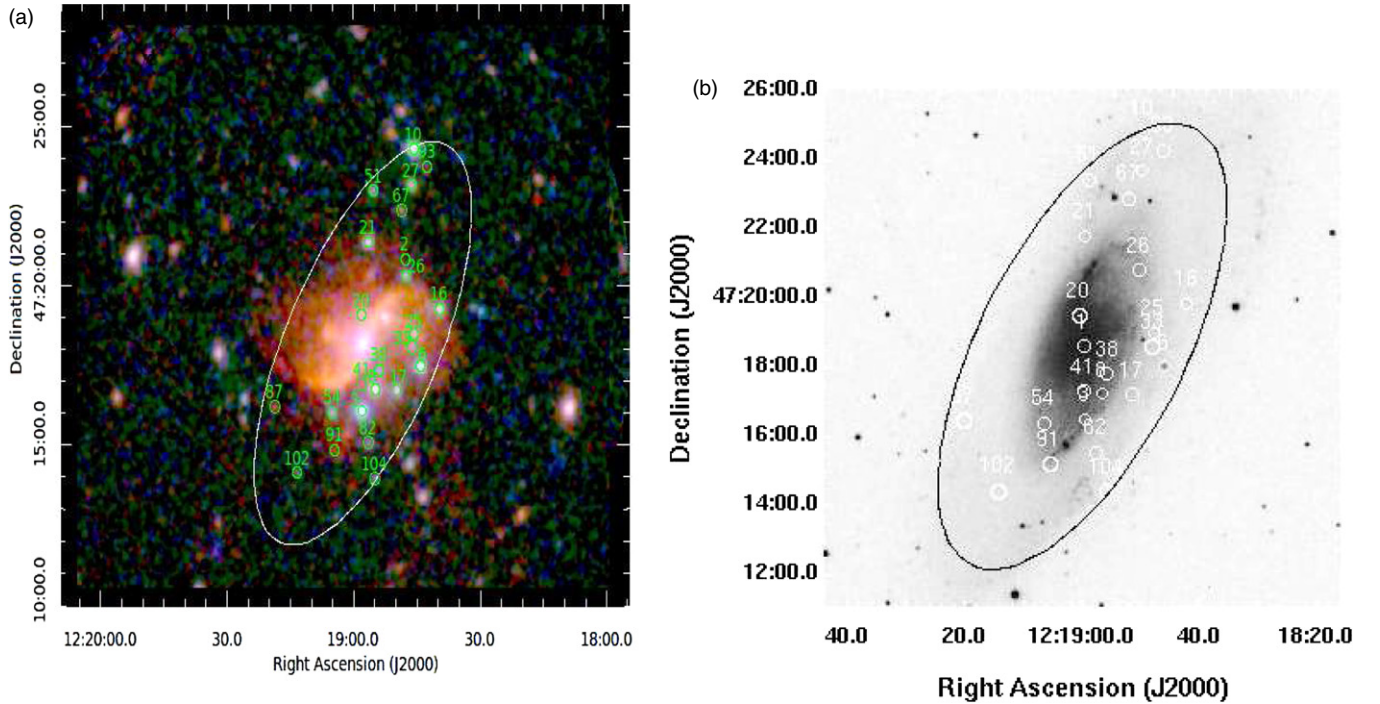


Figure 3. *XMM-Newton* RGB image of NGC 4258. Definitions are the same as in Figure 1.
(A color version of this figure is available in the online journal.)

errors (Column 5), the flux with error (Column 6), and the luminosity with error (Column 7) are given in the (0.2–12) keV band. The luminosities were calculated from the flux values using the distances indicated in Table 1.

2.2. Chandra Observations

To study the spectral and temporal properties of the non-nuclear point sources, we complemented our *XMM-Newton* analysis with *Chandra* data of each target galaxy. A separate observation log of the *Chandra* data is given in Table 7 for

our galaxies. We retrieved the data from the public archive and analyzed the data with the CIAO v4.3 software package using the CALDB v4.4.2 calibration database. All data were filtered to the 0.3–10 keV energy range. The detection of the X-ray point sources was performed using the WAVDETECT task within the same package. We have run the task over the 1, 2, 4, 8 and 16 pixel wavelet scales, since these scales are appropriate for detecting point-like sources. After a visual examination for possible false detections, we have only taken into account the sources with a detection significance of 3.5σ or better and with net counts higher than 6.

Table 4
Parameters of the Sources in NGC 4395 from the *XMM-Newton* Observations

Source	R.A. (J2000) (hh:mm:ss.ss)	Decl. (J2000) (dd:mm:ss.s)	ML	Count Rate (counts s ⁻¹)	Flux (erg cm ⁻² s ⁻¹)	Luminosity (erg s ⁻¹)
XMM-17	12:25:20.49	+33:33:00.8	1.22E+03	1.53E-02 ± 6.3E-04	3.47E-14 ± 1.7E-15	6.24E+37 ± 3.1E+36
XMM-55	12:25:22.18	+33:33:16.9	1.92E+02	5.81E-03 ± 4.5E-04	1.49E-14 ± 1.2E-15	2.68E+37 ± 2.1E+36
XMM-184	12:25:29.06	+33:36:11.4	2.05E+01	1.83E-03 ± 3.2E-04	4.39E-15 ± 9.4E-16	7.90E+36 ± 1.7E+36
XMM-107	12:25:29.26	+33:29:01.3	8.88E+01	3.65E-03 ± 3.8E-04	7.82E-15 ± 1.0E-15	1.40E+37 ± 1.8E+36
XMM-43	12:25:34.45	+33:32:11.8	2.32E+02	4.65E-03 ± 3.5E-04	1.32E-14 ± 1.0E-15	2.37E+37 ± 1.8E+36
XMM-113	12:25:35.28	+33:28:31.5	7.00E+01	3.0E-03 ± 4.2E-04	7.35E-15 ± 1.0E-15	1.32E+37 ± 1.8E+36
XMM-147	12:25:39.25	+33:33:49.8	4.58E+01	1.42E-03 ± 2.0E-04	3.84E-15 ± 6.2E-16	6.91E+36 ± 1.1E+36
XMM-5	12:25:39.55	+33:32:04.1	5.35E+03	3.63E-02 ± 7.5E-04	8.23E-14 ± 2.0E-15	1.48E+38 ± 3.6E+36
XMM-99	12:25:41.09	+33:31:09.4	3.62E+01	1.97E-03 ± 2.7E-04	4.82E-15 ± 7.3E-16	8.67E+36 ± 1.3E+36
XMM-109	12:25:43.63	+33:35:07.0	6.69E+01	1.52E-03 ± 2.0E-04	3.30E-15 ± 5.5E-16	5.94E+36 ± 9.9E+35
XMM-145	12:25:43.79	+33:28:54.4	6.23E+01	2.59E-03 ± 3.0E-04	5.75E-15 ± 8.2E-16	1.03E+37 ± 1.4E+36
XMM-16	12:25:43.95	+33:30:00.2	1.08E+03	1.32E-02 ± 5.2E-04	3.30E-14 ± 1.5E-15	5.94E+37 ± 2.7E+36
XMM-23	12:25:45.11	+33:31:04.6	6.43E+02	7.82E-03 ± 4.0E-04	1.95E-14 ± 1.1E-15	3.51E+37 ± 1.9E+36
XMM-41	12:25:47.05	+33:36:07.4	2.85E+02	5.50E-03 ± 3.6E-04	1.38E-14 ± 1.0E-15	2.48E+37 ± 1.8E+36
XMM-10	12:25:47.20	+33:34:47.4	1.51E+03	1.68E-02 ± 5.5E-04	4.00E-14 ± 1.5E-15	7.20E+37 ± 2.7E+36
XMM-199	12:25:48.70	+33:28:39.3	1.32E+01	1.08E-03 ± 2.1E-04	1.74E-15 ± 5.1E-16	3.13E+36 ± 9.1E+35
XMM-6	12:25:49.00	+33:32:03.5	2.30E+03	4.02E-02 ± 1.1E-03	1.32E-13 ± 3.3E-15	2.37E+38 ± 5.9E+36
XMM-60	12:25:54.08	+33:29:05.9	1.82E+02	4.52E-03 ± 3.4E-04	1.03E-14 ± 9.7E-16	1.85E+37 ± 1.7E+36
XMM-32	12:25:54.44	+33:30:47.0	6.10E+02	1.29E-02 ± 5.8E-04	3.20E-14 ± 1.6E-15	5.76E+37 ± 2.8E+36
XMM-114	12:25:57.32	+33:29:47.1	5.50E+01	2.50E-03 ± 3.1E-04	6.17E-15 ± 9.2E-16	1.11E+37 ± 1.6E+36
XMM-66	12:25:57.35	+33:30:39.8	8.77E+01	2.31E-03 ± 2.5E-04	4.42E-15 ± 7.2E-16	7.95E+36 ± 1.3E+36
XMM-155	12:25:57.98	+33:36:09.8	1.34E+01	1.05E-03 ± 2.2E-04	2.88E-15 ± 6.2E-16	5.18E+36 ± 1.1E+36
XMM-100	12:25:58.87	+33:28:23.7	9.08E+01	3.68E-03 ± 3.6E-04	8.71E-15 ± 1.0E-15	1.56E+37 ± 1.8E+36
XMM-24	12:25:59.79	+33:33:22.0	5.43E+01	5.82E-03 ± 5.6E-04	1.35E-14 ± 1.5E-15	2.43E+37 ± 2.7E+36
XMM-2	12:26:01.42	+33:31:32.0	1.34E+05	4.15E-01 ± 2.3E-03	9.12E-13 ± 6.2E-15	1.64E+39 ± 1.1E+37
XMM-86	12:26:04.10	+33:32:50.6	6.42E+01	1.85E-03 ± 3.4E-04	7.96E-15 ± 9.7E-16	1.43E+37 ± 1.7E+36
XMM-201	12:26:13.79	+33:33:45.9	1.36E+01	1.47E-03 ± 2.6E-04	3.79E-15 ± 7.4E-16	6.82E+36 ± 1.3E+36
XMM-215	12:26:15.83	+33:33:48.0	1.44E+01	1.28E-03 ± 2.4E-04	2.80E-15 ± 6.5E-16	5.04E+36 ± 1.1E+36
XMM-135	12:26:16.42	+33:30:18.2	3.74E+01	1.81E-03 ± 2.6E-04	4.05E-15 ± 7.3E-16	7.29E+36 ± 1.3E+36

Notes. The sources are ordered by increasing right ascension (R.A.). Column 1: source ID; Column 2 and 3: source coordinates; Column 4: likelihood of existence; Column 5: integrated EPIC-pn and MOS count rates and errors in the 0.2–12 keV band; Columns 6 and 7: flux and luminosity in the 0.2–12 keV band.

Table 5
Parameters of the Sources in NGC 4736 from the *XMM-Newton* Observations

Source	R.A. (J2000) (hh:mm:ss.ss)	Decl. (J2000) (dd:mm:ss.s)	ML	Count Rate (counts s ⁻¹)	Flux (erg cm ⁻² s ⁻¹)	Luminosity (erg s ⁻¹)
XMM-58	12:50:27.02	+41:05:07.5	7.49E+01	6.47E-03 ± 9.1E-04	3.30E-15 ± 1.2E-15	6.89E+36 ± 2.5E+36
XMM-31	12:50:33.10	+41:05:12.8	1.48E+02	9.58E-03 ± 8.5E-04	2.30E-14 ± 2.4E-15	4.80E+37 ± 5.0E+36
XMM-73	12:50:34.93	+41:07:43.7	3.16E+01	3.94E-03 ± 5.7E-04	7.76E-15 ± 1.4E-15	1.62E+37 ± 2.9E+36
XMM-19	12:50:35.25	+41:10:26.4	2.42E+02	1.086E-02 ± 8.3E-04	2.92E-14 ± 2.4E-15	6.10E+37 ± 5.0E+36
XMM-63	12:50:35.73	+41:06:43.9	3.54E+01	3.81E-03 ± 5.8E-04	1.08E-14 ± 1.7E-15	2.25E+37 ± 3.5E+36
XMM-76	12:50:37.69	+41:10:37.9	3.48E+01	3.80E-03 ± 5.7E-04	9.42E-15 ± 1.6E-15	1.96E+37 ± 3.3E+36
XMM-12	12:50:47.72	+41:05:10.8	5.28E+02	1.95E-02 ± 1.0E-03	4.45E-15 ± 2.8E-15	9.30E+36 ± 5.8E+36
XMM-41	12:50:48.00	+41:08:35.1	2.25E+01	4.29E-03 ± 6.6E-04	9.24E-15 ± 1.7E-15	1.93E+37 ± 3.5E+36
XMM-2	12:50:48.64	+41:07:40.5	4.77E+04	5.62E-01 ± 4.4E-03	1.31E-12 ± 1.2E-14	2.73E+39 ± 2.5E+37
XMM-72	12:50:50.14	+41:11:29.4	2.39E+01	3.00E-03 ± 5.3E-04	8.41E-15 ± 1.5E-15	1.75E+37 ± 3.1E+36
XMM-3	12:50:50.27	+41:07:10.1	2.63E+03	1.39E-01 ± 2.8E-03	3.31E-13 ± 7.9E-15	6.91E+39 ± 1.6E+37
XMM-36	12:50:52.57	+41:02:52.7	1.92E+02	9.27E-03 ± 8.5E-04	2.18E-14 ± 2.3E-15	4.55E+37 ± 4.8E+36
XMM-24	12:50:53.00	+41:08:43.5	1.06E+01	3.41E-03 ± 6.8E-04	8.63E-15 ± 1.8E-15	1.80E+37 ± 3.7E+36
XMM-56	12:50:53.48	+41:04:55.2	4.19E+01	4.40E-03 ± 5.8E-04	9.79E-15 ± 1.5E-15	2.04E+37 ± 3.1E+36
XMM-6	12:50:53.67	+41:06:34.2	3.57E+02	7.34E-02 ± 3.5E-03	1.67E-13 ± 9.6E-15	3.49E+38 ± 2.0E+37
XMM-39	12:50:54.24	+41:09:06.4	4.94E+01	3.35E-03 ± 4.6E-04	5.70E-15 ± 1.1E-15	1.19E+37 ± 2.2E+36
XMM-4	12:50:56.10	+41:06:55.9	3.55E+03	4.16E-01 ± 7.4E-03	9.44E-13 ± 2.0E-14	1.97E+39 ± 4.1E+37
XMM-11	12:50:59.87	+41:02:53.8	5.45E+02	8.49E-03 ± 6.4E-04	3.70E-15 ± 9.6E-15	7.73E+36 ± 2.0E+37
XMM-44	12:51:02.00	+41:03:04.7	9.74E+01	5.98E-03 ± 6.2E-04	1.51E-14 ± 1.8E-15	3.15E+37 ± 3.7E+36
XMM-18	12:51:04.43	+41:07:26.0	2.10E+02	9.90E-03 ± 7.6E-04	2.67E-14 ± 2.2E-15	5.58E+37 ± 4.5E+36
XMM-27	12:51:09.01	+41:02:57.8	2.37E+02	9.96E-03 ± 7.7E-04	2.63E-14 ± 2.2E-15	5.49E+37 ± 4.5E+36

Note. Definitions are the same as in Table 3.

Table 6
Parameters of the Sources in NGC 4258 from the *XMM-Newton* Observations

Source	R.A. (J2000) (hh:mm:ss.ss)	Decl. (J2000) (dd:mm:ss.s)	ML	Count Rate (counts s ⁻¹)	Flux (erg cm ⁻² s ⁻¹)	Luminosity (erg s ⁻¹)
XMM-16	12:18:39.38	+47:19:19.1	2.37E+03	5.02E-02 ± 1.4E-03	1.23E-13 ± 3.9E-15	7.19E+38 ± 2.2E+37
XMM-93	12:18:42.24	+47:23:46.9	4.19E+01	3.15E-03 ± 5.2E-04	7.33E-15 ± 1.5E-15	4.28E+37 ± 8.7E+36
XMM-6	12:18:43.94	+47:17:31.7	6.91E+03	8.78E-02 ± 1.6E-03	2.16E-13 ± 4.5E-15	1.26E+39 ± 2.6E+37
XMM-25	12:18:45.44	+47:18:32.1	1.28E+03	1.22E-01 ± 3.4E-03	3.06E-13 ± 9.7E-15	1.79E+39 ± 5.6E+37
XMM-10	12:18:45.48	+47:24:20.5	5.06E+03	7.96E-02 ± 1.8E-03	2.15E-13 ± 5.6E-15	1.25E+39 ± 3.2E+37
XMM-33	12:18:45.78	+47:18:07.5	3.44E+01	6.05E-03 ± 7.7E-04	1.40E-14 ± 2.0E-15	8.19E+37 ± 1.1E+37
XMM-27	12:18:46.00	+47:23:12.9	7.49E+02	1.94E-02 ± 9.2E-04	4.45E-14 ± 2.5E-15	2.60E+38 ± 1.4E+37
XMM-26	12:18:47.29	+47:20:22.0	4.09E+02	1.47E-02 ± 8.2E-04	3.59E-14 ± 2.2E-15	2.10E+38 ± 1.2E+37
XMM-2	12:18:47.57	+47:20:53.8	3.26E+04	1.64E-01 ± 4.1E-03	4.44E-13 ± 1.2E-14	2.59E+39 ± 7.0E+37
XMM-67	12:18:48.46	+47:22:26.1	8.41E+01	5.10E-03 ± 5.4E-04	1.02E-14 ± 1.4E-15	5.96E+37 ± 8.1E+36
XMM-17	12:18:49.55	+47:16:46.6	1.41E+03	3.29E-02 ± 1.0E-03	8.13E-14 ± 3.0E-15	4.75E+38 ± 1.7E+37
XMM-38	12:18:53.68	+47:17:24.5	8.64E+01	7.18E-03 ± 7.4E-04	1.98E-14 ± 2.1E-15	1.15E+38 ± 1.2E+37
XMM-8	12:18:54.72	+47:16:49.4	4.93E+03	9.35E-02 ± 1.8E-03	2.43E-13 ± 5.6E-15	1.42E+39 ± 3.2E+37
XMM-104	12:18:54.79	+47:13:59.7	2.24E+01	2.23E-03 ± 4.6E-04	6.46E-15 ± 1.4E-15	3.77E+37 ± 8.1E+36
XMM-51	12:18:55.14	+47:23:02.5	1.90E+02	8.50E-03 ± 6.6E-04	2.13E-14 ± 1.8E-15	1.24E+38 ± 1.0E+37
XMM-82	12:18:56.27	+47:15:08.1	5.03E+01	4.15E-03 ± 5.1E-04	8.74E-15 ± 1.3E-15	5.11E+37 ± 7.6E+36
XMM-21	12:18:56.34	+47:21:25.6	1.46E+03	3.00E-02 ± 1.0E-03	7.15E-14 ± 2.8E-15	4.18E+38 ± 1.6E+37
XMM-41	12:18:57.93	+47:16:56.7	1.70E+01	2.68E-03 ± 4.4E-04	5.94E-15 ± 1.1E-15	3.47E+37 ± 6.4E+36
XMM-3	12:18:57.94	+47:16:07.7	1.36E+04	1.33E-01 ± 1.9E-03	3.37E-13 ± 5.5E-15	1.97E+39 ± 3.2E+37
XMM-20	12:18:57.96	+47:19:07.4	9.25E+01	1.40E-02 ± 1.2E-03	3.13E-14 ± 3.2E-15	1.83E+38 ± 1.8E+37
XMM-91	12:19:04.35	+47:14:53.3	5.58E+01	3.36E-03 ± 5.1E-04	8.06E-15 ± 1.4E-15	4.71E+37 ± 8.1E+36
XMM-54	12:19:04.90	+47:16:03.9	1.53E+02	5.02E-03 ± 4.8E-04	9.43E-15 ± 1.3E-15	5.51E+37 ± 7.6E+36
XMM-102	12:19:13.23	+47:14:11.2	2.59E+01	2.87E-03 ± 4.2E-04	7.90E-15 ± 1.3E-15	4.62E+37 ± 7.6E+36
XMM-87	12:19:18.59	+47:16:14.7	3.12E+01	2.66E-03 ± 4.0E-04	5.57E-15 ± 1.0E-15	3.25E+37 ± 5.8E+36

Note. Definitions are the same as in Table 3.

Table 7
The Log of *Chandra* Observations for the Three Galaxies Studied

Galaxy	ObsId	Obs. Date	Exposure (ks)	Instrument
NGC 4395	882	2000.06.20	20.0	ACIS-S
NGC 4736	808	2000.05.13	50.0	ACIS-S
	9553	2008.02.16	25.7	ACIS-I
NGC 4258	350	2000.04.17	14.5	ACIS-S
	1618	2001.05.28	22.0	ACIS-S
	2340	2001.05.29	7.0	ACIS-S

It is well known that *Chandra* has significantly better angular resolution than *XMM-Newton*. As a result, the detected *XMM-Newton* point sources (one or two) in the central region of galaxies may have overlapped several *Chandra* point sources. Since in the present analyses we examined only the non-nuclear sources, the sources located in the central regions with a 0.3 radius were excluded in all three galaxies.

We have started our *Chandra* data analysis with NGC 4395 and the detected 11 point sources in its D_{25} region. Only one source in the central region of the galaxy has been excluded. From the remaining 10, several have corresponding *XMM-Newton* sources. Four of them were examined individually in Section 5.1 due to sufficient statistics provided by *XMM-Newton* observations. These four *Chandra* source positions are offset within 2'' of the *XMM-Newton* source positions in the center of the galaxy.

When the same procedure was carried out for the other two galaxies we obtained the following: For NGC 4736, 43 point sources in the D_{25} region were detected. Fifteen sources that were in the central region have been excluded. From the remaining 28 several were overlapped by *XMM-Newton*

sources. Among them, three sources coincided with *XMM-Newton* sources, which are examined individually in Section 5.2. The *XMM-Newton* and *Chandra* source positions of these three agree within 2'' in NGC 4736.

For NGC 4258, 42 point sources were detected in the D_{25} region. Five point sources in the central region have been removed. Among the remaining sources, six have corresponding *XMM-Newton* sources, and they are examined individually in Section 5.3. The *XMM-Newton* and *Chandra* source positions of these six agree within $\sim < 1''$ (except XMM-8 with two *Chandra* sources within its 15'' *XMM-Newton* error circle).

3. SPECTRAL ANALYSIS

To perform a spectral analysis for each luminous source, corresponding data were extracted from a circular region with a radius of (15''–20'') for pn, MOS1, and MOS2 depending on the presence of nearby sources. Background events were extracted from a source-free zone normalized to the source extraction area.

The source spectra with the instrument responses and ancillary files were generated using the SAS version 10.0. The spectral analyses of the X-ray data have been performed using XSPEC version 12.5. We grouped the pn and MOS spectral energy channels to have at least 20–30 counts per bin for good statistical quality in the spectra. Initially we fitted the spectra with four different one-component models: blackbody (BBODY), power law (PL), diskblackbody (DISKBB), and bremsstrahlung (BREMSS). In addition, we applied the following two-component models: powerlaw+blackbody (PL+BBODY), powerlaw+disk blackbody (PL+DISKBB), and powerlaw+mekal (PL+MEKAL). We also used a photoelectric absorption model as part of the fit. The fits were applied to data in the 0.2–10 keV range.

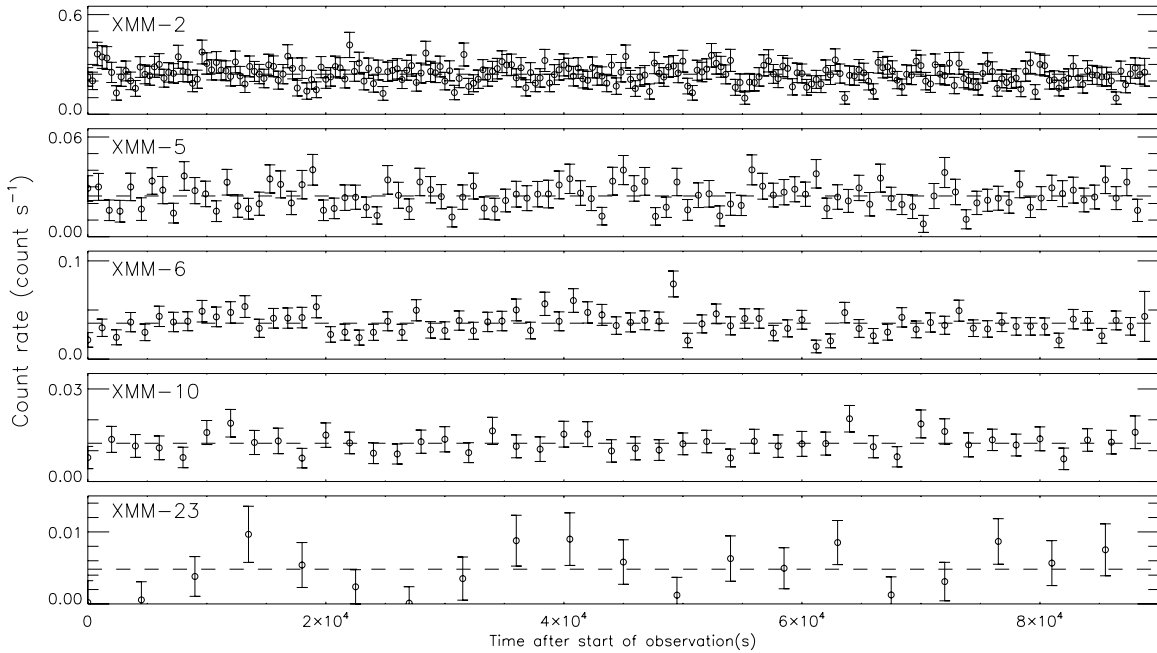


Figure 4. *XMM-Newton* short-term light curves of NGC 4395 point sources. These light curves were obtained from the counts using only the EPIC-pn camera. The dashed line shows the mean count rate and error bars correspond to 1σ deviations assuming Gaussian statistics.

The EPIC-pn and MOS spectra were fitted simultaneously for each object only in galaxies NGC 4736 and NGC 4258. For NGC 4395 we used only the EPIC-pn data due to the low statistical quality of the MOS data. We used a constant parameter that was set free to account for the normalization differences in the flux calibration of the three EPIC cameras.

To compare the spectral shapes of sources between *XMM-Newton* and *Chandra* observations, we fitted the same spectral models to all data. Each data set was chosen based on a longer exposure time to provide sufficient counts for spectral fitting. Standard CIAO routines were used to reprocess event lists; then source and background spectra were extracted to construct the so-called RMF and ARF files. We have fitted the data of 13 *Chandra* sources in the three galaxies; however, only two of them (XMM-3 and XMM-6 in NGC 4258) were above the threshold (>300 counts) for spectral analysis. Our results are consistent with the *XMM-Newton* analysis and therefore we have discussed only the spectral parameters of these two sources in NGC 4258 in Section 5.3.

4. TIMING ANALYSIS

X-ray variability of sources in all three galaxies was tested by deriving their short-term (based on the observation with the longest exposure available) and long-term light curves. For short-term variability, the data from EPIC-pn and MOS cameras were added to improve S/N. After excluding the high background flaring, the corrected exposure times were binned in the range from 200 to 4500 s and each bin had at least 20 counts after background subtraction.

We applied a χ^2 test to search for large amplitude variations with respect to the constant count rate hypothesis. Short-term variability of point sources for each galaxy in our list can be followed from Figures 4, 5, and 6, respectively. In Table 8 we present the results of χ^2 tests together with $P(\text{var})$, the probability values for those cases exceeding the 95% taken as the limit for variability. The results are such that, in NGC 4395

Table 8
XMM-Newton Short-term Source Variability χ^2 Test Results
for the Three Galaxies Studied

Galaxy	Source	Bin Size (s)	χ^2 Statistic	
			χ^2/dof	$P_{\chi^2}(\text{var})$
NGC 4395	XMM-2	400	254/222	...
	XMM-5	900	114/98	...
	XMM-6	1200	100/74	97.6%
	XMM-10	2000	29/44	...
	XMM-23	4500	23/19	...
NGC 4736	XMM-2	200	880/194	$>99.9\%$
	XMM-12	2200	17/17	...
	XMM-18	3000	9/12	...
NGC 4258	XMM-2	900	55/27	$>99.9\%$
	XMM-3	700	155/91	$>99.9\%$
	XMM-6	750	223/85	$>99.9\%$
	XMM-8	1100	94/58	99.8%
	XMM-10	1500	47/42	...
	XMM-16	1500	68/42	99.3%
	XMM-17	2500	41/25	97.7%
	XMM-21	2000	142/32	$>99.9\%$

one out of five, and in NGC 4736 one out of three, sources are variable while in NGC 4258 variable sources increased to seven out of eight. Kolmogorov–Smirnov tests were also applied to search for small amplitude variations in the source count rates; however, nothing significant was found.

For long-term variability, in addition to *XMM-Newton* and *Chandra*, *ROSAT* data from the literature were also added to the analysis, all in the 0.5–2 keV energy range. In this application, to calculate *XMM-Newton* fluxes, data were fitted with their best-fitting models and fluxes were calculated after the spectra of the sources determined.

For *Chandra* source fluxes, even though the data for 11 out of 13 sources were below the threshold (as noted above), for

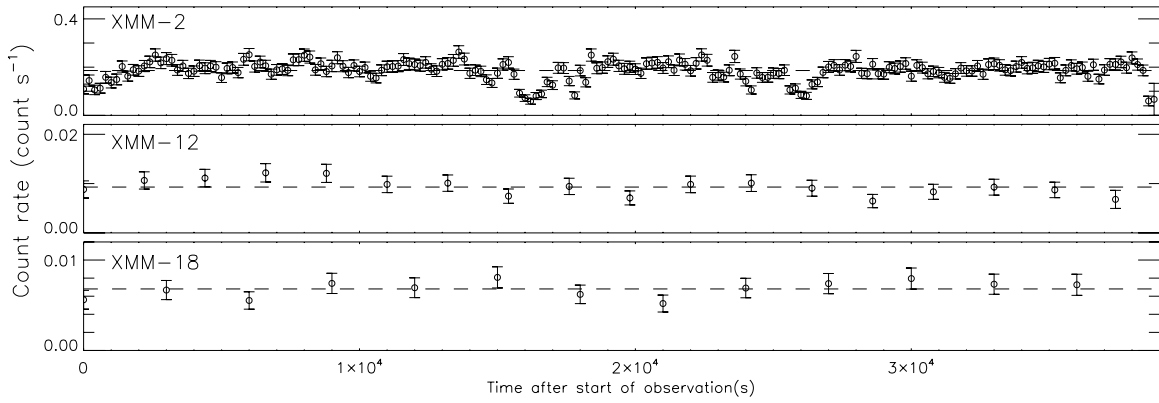


Figure 5. *XMM-Newton* short-term light curves of NGC 4736 point sources. These light curves were obtained by summing the counts from the EPIC-pn and MOS cameras. The dashed line shows the mean count rate and error bars correspond to 1σ deviations assuming Gaussian statistics.

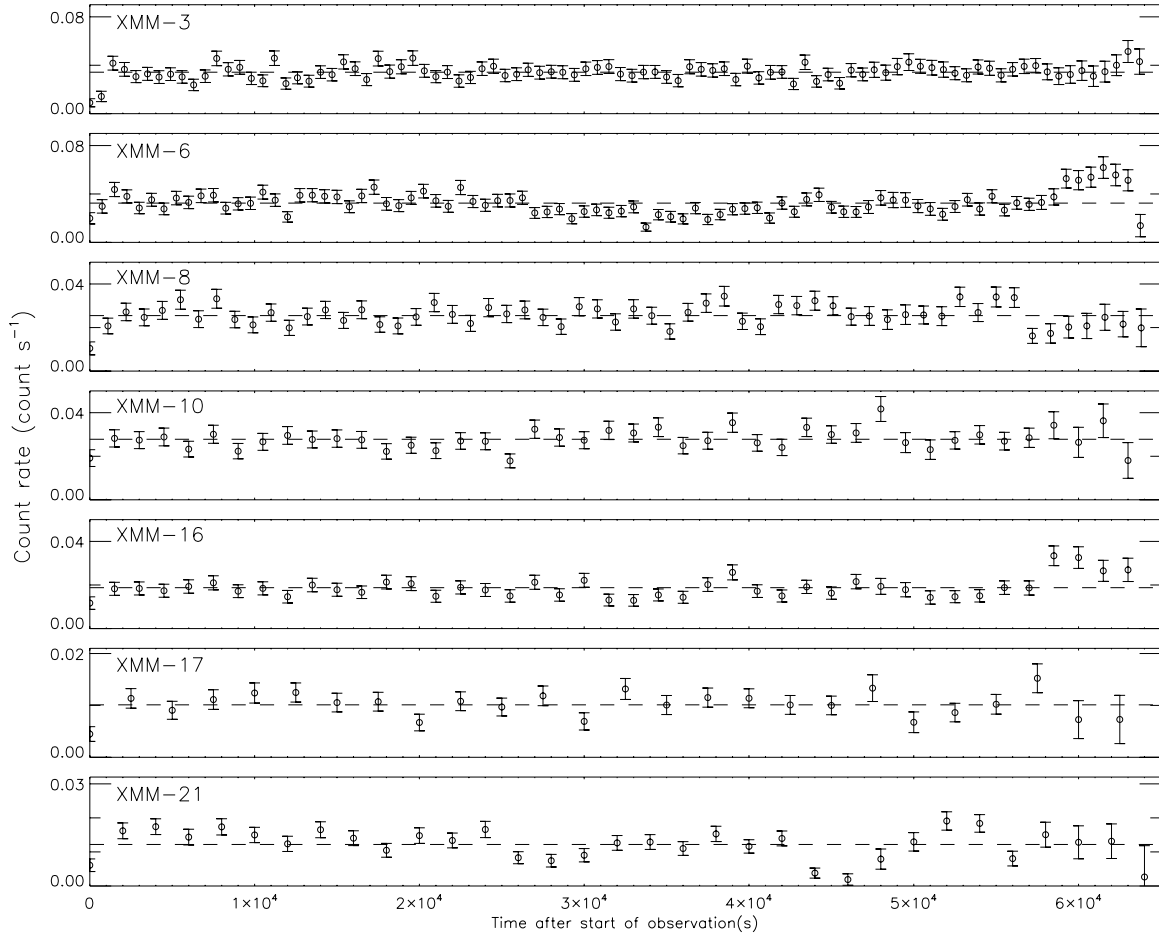


Figure 6. *XMM-Newton* short-term light curves of NGC 4258 point sources. These light curves were obtained by summing the counts from the EPIC-pn and MOS cameras. The dashed line shows the mean count rate and error bars correspond to 1σ deviations assuming Gaussian statistics.

comparison purposes we have tried to fit the data with the same best-fitting *XMM-Newton* model with no constraint on *Chandra* data fit parameters. We have succeeded in getting flux values for only two sources in NGC 4395 (XMM-5 and XMM-6), two sources in NGC 4736 (XMM-2 and XMM-12), and five sources in NGC 4258 (XMM-3, XMM-6, XMM-16, XMM-17, and XMM-21) within the same energy range (0.5–2) keV. In our timing analysis, we used the longer exposure time if the data were obtained within a year.

To derive fluxes for *ROSAT* observations, count rates available from the literature were used. The absorbed PL continuum slope

value was taken from the *XMM-Newton* observation and the standard *WebPIMMS* was used to calculate flux.

The resulting long-term light curves for sources in all three galaxies are shown in Figures 7(a)–(c). For the transient ULX source in NGC 4258, short- and long-term light curves are shown in Figures 8(a) and (b). Here, the total number of points of observation for the long time interval (18 months to 12 years) looks rather sparse. However, there are noticeable indications of long-term variability for a number of sources studied. Our variability search for individual sources in each galaxy will be discussed further in the following sections.

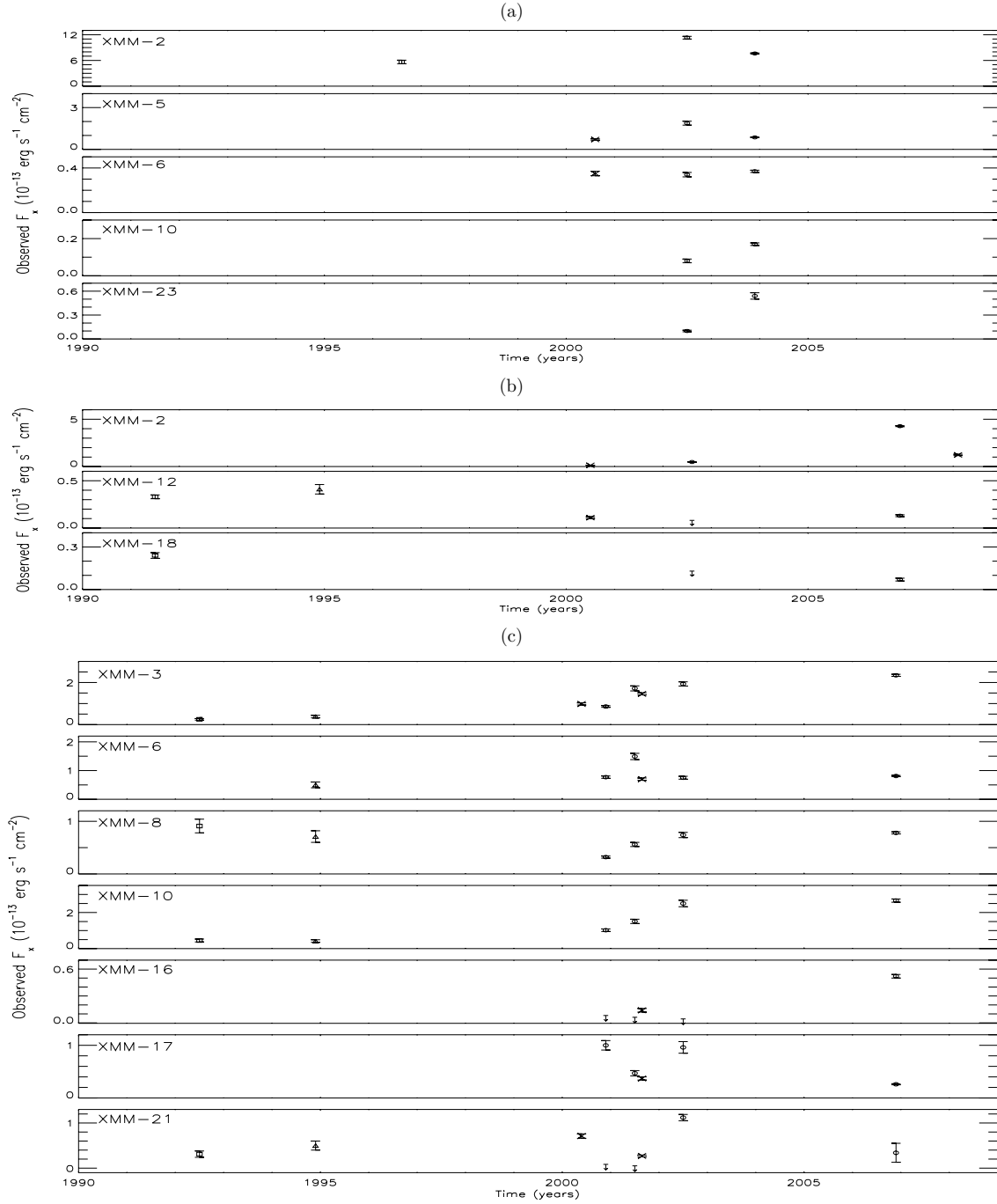


Figure 7. *XMM-Newton* long-term light curves of NGC 4395, NGC 4736, and NGC 4258 are shown in panels (a), (b), and (c), respectively. The data points taken from *XMM-Newton* (circles), *ROSAT/PSPC* (squares), *ROSAT/HRI* (triangles), and *Chandra* (stars) flux measurements have been converted to the (0.5–2) keV flux as explained in the text. Flux upper limits are shown with downward arrows.

5. INDIVIDUAL SOURCE PROPERTIES

In this section, we discuss observations of each galaxy individually, highlighting the spectral and timing properties of X-ray luminous point sources in turn.

5.1. NGC 4395

This galaxy was observed in 2002 and 2003 (see Table 2). Within the D_{25} region, we have detected 29 point sources as given in Table 3. Our detection limiting flux in the 0.2–12 keV energy band is $\sim 1.2 \times 10^{-15} \text{ erg cm}^{-2} \text{ s}^{-1}$ for sources inside the optical disk. The best-fitting model spectra for five sources

were obtained by using only the pn data since the MOS data had rather poor statistics. In our further analysis, we obtained the best-fitting spectral parameters for one-component and two-component models for the five sources. Our results are summarized in Tables 9 and 10, respectively, together with unabsorbed fluxes and luminosities in the energy range 0.2–10 keV. The best-fitting model spectra of these sources are given in Figure 9. We elaborate on their individual spectral characteristics below.

XMM-2. This is the brightest object in the galaxy and is about 2.9 away from the galaxy center. It is located near a giant H II region complex. The distance between the position of the source,

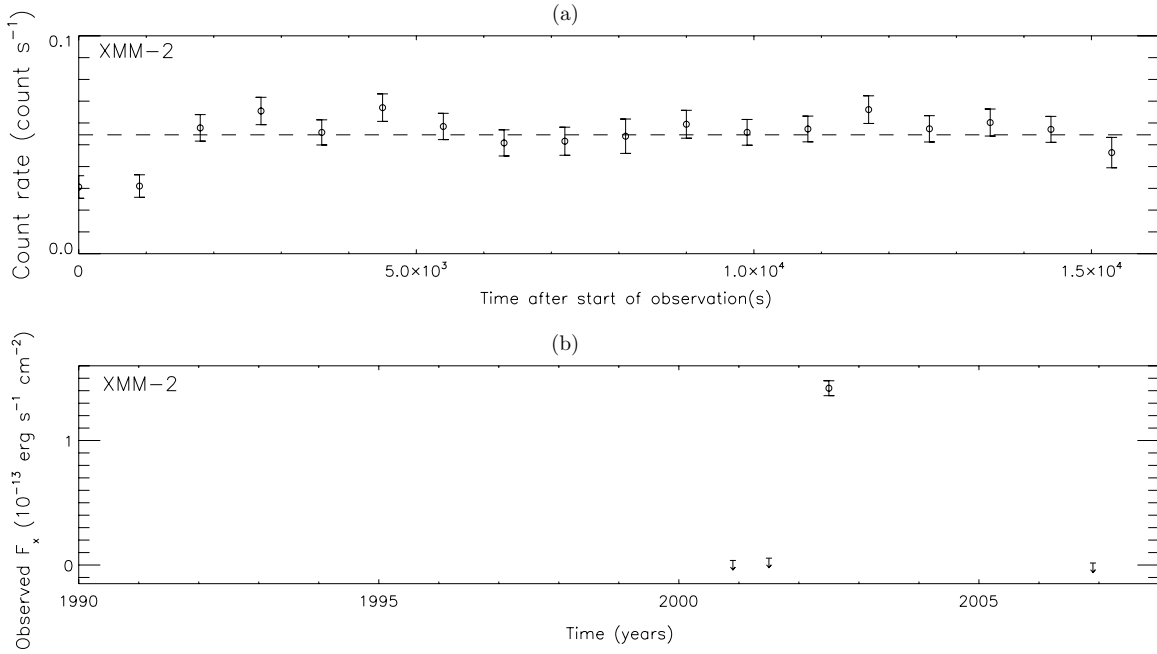


Figure 8. (a) Short-term and (b) long-term light curves of XMM-2 in NGC 4258. The properties and possible nature of this transient source are described in the text.

Table 9
Spectral Parameters Obtained with One-component Model Fits for Point Sources in NGC 4395

Source	Model	N_H (10^{22} cm^{-2})	Γ	kT (keV)	χ^2/dof	F (10^{-13}) ($\text{erg cm}^{-2} \text{ s}^{-1}$)	L (10^{38}) (erg s^{-1})
XMM-2	BBODY	$0.03^{+0.01}_{-0.01}$		$0.20^{+0.006}_{-0.007}$	253.60/142	3.43	6.20
	PL	$0.26^{+0.03}_{-0.03}$	$4.27^{+0.26}_{-0.23}$		209.13/142	6.36	11.51
	DISKBB	$0.07^{+0.01}_{-0.01}$		$0.26^{+0.01}_{-0.01}$	224.29/142	5.23	9.46
	BREMSS	$0.12^{+0.02}_{-0.01}$		$0.47^{+0.04}_{-0.04}$	206.86/142	8.37	15.14
XMM-5	BBODY	0.04		0.26	137.22/58	0.39	0.70
	PL	0.31	3.62		128.66/58	4.27	7.72
	DISKBB	0.18		0.67	129.77/58	0.93	0.68
	BREMSS	0.12		0.35	127.49/58	0.58	1.05
	VPSHOCK	$0.06^{+0.02}_{-0.01}$		$3.98^{+2.20}_{-0.91}$	106.32/71	0.52	1.08
XMM-6	BBODY	0.00		0.59	188.68/56	0.71	1.28
	PL	$0.06^{+0.02}_{-0.02}$	$1.42^{+0.09}_{-0.09}$		63.32/56	1.45	2.62
	DISKBB	0.03		$1.89^{+0.20}_{-0.35}$	74.58/56	1.20	2.17
	BREMSS	$0.04^{+0.02}_{-0.01}$		$18.9^{+18.00}_{-7.50}$	62.18/56	1.37	2.47
XMM-10	BBODY	0.00		0.47	59.16/29	0.19	0.34
	PL	$0.15^{+0.04}_{-0.05}$	$1.86^{+0.15}_{-0.17}$		27.12/29	0.51	0.92
	DISKBB	0.02		$1.22^{+0.30}_{-0.24}$	33.81/29	0.31	0.56
	BREMSS	$0.01^{+0.04}_{-0.03}$		$5.39^{+4.03}_{-1.80}$	31.21/29	0.40	0.72
XMM-23	BBODY	$0.28^{+0.22}_{-0.01}$		$0.06^{+0.03}_{-0.02}$	12.94/10	0.33	0.60
	PL	$0.17^{+0.14}_{-0.14}$	$6.87^{+2.30}_{-1.83}$		12.49/10	0.98	0.17
	DISKBB	$0.17^{+0.08}_{-0.06}$		$0.09^{+0.02}_{-0.02}$	11.57/10	0.62	0.27
	BREMSS	$0.21^{+0.07}_{-0.05}$		$0.12^{+0.10}_{-0.08}$	11.67/10	0.61	0.23

Note. The best-fitting model for each source is highlighted in bold.

XMM-2, and the center of the nearby H II region is no less than ~ 500 pc. This calculation takes into account a deprojected distance using the inclination of the galaxy. (The distribution of H II regions in this galaxy was studied by Cedres & Cepa (2002) in detail.) The source spectrum obtained using *XMM-Newton* data is not adequately fitted with any one-component model. The

best-fitting two-component model is an absorbed PL + DISKBB ($\Gamma = 3.11$, $T_{\text{in}} = 0.19$ keV). But a PL+MEKAL model provides an almost identical fit ($\chi^2_{\nu} = 1.2$) with similar parameters. It has an unabsorbed luminosity of $L_X = 2.2 \times 10^{39} \text{ erg s}^{-1}$, which is within the standard ULX limit. Both short-term and long-term light curves do not show evidence of variability. However, its

Table 10
Spectral Parameters Obtained Using Two-component Model Fits for Point Sources in NGC 4395

Source	Model	N_{H} (10^{22} cm^{-2})	Γ	kT (keV)	χ^2/dof	F (10^{-13}) ($\text{erg cm}^{-2} \text{ s}^{-1}$)	L (10^{38}) (erg s^{-1})
XMM-2	PL+BBODY	$0.29^{+0.04}_{-0.04}$	$4.41^{+0.32}_{-0.29}$	$0.09^{+2.74}_{-0.004}$	206.75/140	12.8	23.16
	PL+DISKBB	$0.15^{+0.04}_{-0.03}$	$3.11^{+0.43}_{-0.36}$	$0.19^{+0.02}_{-0.02}$	171.80/140	12.3	22.26
	PL+MEKAL	$0.18^{+0.03}_{-0.02}$	$3.80^{+0.19}_{-0.15}$	$0.64^{+0.07}_{-0.07}$	168.06/140	23.1	41.81
XMM-5	PL+BBODY	$0.12^{+0.03}_{-0.05}$	$1.71^{+0.65}_{-0.56}$	$0.20^{+0.02}_{-0.03}$	98.02/56	0.72	1.30
	PL+DISKBB	0.28	3.44	0.06	128.78/56	0.08	0.14
	PL+MEKAL	$0.42^{+0.05}_{-0.08}$	$3.40^{+0.41}_{-0.20}$	$0.17^{+0.02}_{-0.02}$	88.59/56	5.96	10.78
XMM-6	PL+BBODY	$0.05^{+0.08}_{-0.04}$	$1.40^{+0.10}_{-0.09}$	199.36	61.73/54	1.45	2.67
	PL+DISKBB	$0.04^{+0.04}_{-0.03}$	$1.34^{+1.91}_{-0.42}$	$1.25^{+1.25}_{-1.25}$	60.30/54	1.37	2.47
	PL+MEKAL	$0.14^{+0.11}_{-0.04}$	$4.43^{+1.25}_{-1.56}$	$14.16^{+20.25}_{-5.75}$	56.21/54	2.36	4.27
XMM-10	PL+BBODY	$0.16^{+0.09}_{-0.06}$	$1.95^{+0.33}_{-0.50}$	$28.88^{+28.90}_{-28.90}$	26.80/27	0.56	1.01
	PL+DISKBB	$0.14^{+0.06}_{-0.03}$	$1.83^{+0.30}_{-0.20}$	0.005	26.78/27	0.03	0.04
	PL+MEKAL	$0.13^{+0.05}_{-0.06}$	$1.66^{+0.32}_{-0.20}$	$0.60^{+0.22}_{-0.41}$	22.11/27	4.94	8.94
XMM-23	PL+BBODY	$0.30^{+0.26}_{-0.11}$	$7.17^{+7.17}_{-2.05}$	$2.19^{+2.19}_{-2.19}$	9.94/8	18.68	33.81
	PL+DISKBB	1.05	0.90	0.12	19.80/8	0.10	0.18
	PL+MEKAL	$0.26^{+0.26}_{-0.17}$	$6.55^{+6.55}_{-7.46}$	$0.08^{+0.18}_{-0.08}$	10.06/8	6.66	12.04

Note. The best-fitting model for each source is highlighted in bold.

spectral shape and high luminosity lead us to conclude that it is a ULX. This source was claimed earlier to be a ULX by Stobbart et al. (2006). XMM-2 was also defined as a ULX with the best-fitted two-component model, BB+PL ($\Gamma = 3.44$, $kT = 0.14 \text{ keV}$), using 2000 and 2002 archival data by Winter et al. (2006, hereafter WMR2006). We think that this ULX source requires deeper observations to decide better its spectral and temporal characteristics.

XMM-5. This is the most notable source in this galaxy. We derived a source spectrum and fitted this spectrum with a VPSHOCK model (another XSPEC model) of a non-equilibrium, ionization plasma emission as suitable for SNRs (Borkowski et al. 1996). The resulting spectral parameters are $kT = 3.98 \text{ keV}$ with an unabsorbed luminosity of $L_X \sim 1.1 \times 10^{38} \text{ erg s}^{-1}$. The light curve for XMM-5 shows no variability on both long and short timescales; this is expected since it is an SNR candidate, the only one in our entire source catalog with a possibly extended nature.

To explore this unique possibility, we also conducted an optical spectroscopic observation to confirm and clarify its nature. In order to differentiate SNRs from typical H II regions, we used the well-known criterion $[\text{S II}]/\text{H}\alpha \geq 0.4$ proposed by Mathewson & Clarke (1973). The spectral data were obtained by the TFOSC (TUG Faint Object Spectrograph and Camera) instrument mounted on RTT150 (Russian–Turkish Telescope at Antalya, Turkey) in 2009 April. The optical spectrum of the source is given in Figure 10. In Table 11 observed line intensities, the $E_{(B-V)}$, and $\text{H}\alpha$ intensity values are listed. As these optical observations reveal, this source is indeed an SNR rather than a ULX as claimed by Swartz et al. (2004). In a more recent study of this galaxy, the SNR nature of XMM-5 was also discussed by Leonidaki et al. (2010) using higher resolution *Chandra* archival data.

XMM-6 and XMM-10. The spectra of these sources are best fitted with an absorbed PL model with a photon index of $\Gamma = 1.42$ and $\Gamma = 1.86$, respectively. Quite similar luminosity values of $L_X = 2.6 \times 10^{38} \text{ erg s}^{-1}$ and $\sim 1 \times 10^{38} \text{ erg s}^{-1}$ are

Table 11
Relative Line Intensities and Spectroscopic Parameters Obtained from TUG Observations for the SNR Candidate Source XMM-5 in NGC 4395

Line	XMM-5	
H α ($\lambda 6563$)	100	
S II($\lambda 6716$)	30.8	
S II($\lambda 6731$)	11.3	
O I($\lambda 6300$)	221.7	
O II($\lambda \lambda 7320, 7330$)	413	
$E_{(B-V)}$	0.02	
I(H α)	2.3E-13	$\text{erg cm}^{-2} \text{ s}^{-1}$
(S II($\lambda 6716$)+S II($\lambda 6731$))/H α	0.42	

also observed, respectively. These two sources are at different distances from the central bulge of the galaxy; however, we think that XMM-6 has a noticeable contribution from the galactic bulge material, which may explain the differences in spectral shapes and luminosities. We detected no definite variation in the long-term light curve of XMM-6, but its short-term light curve satisfies our criteria of variability. XMM-10 does not show any definite indication of short-term variability, although its long-term light curve does show some variability (a factor of ~ 2). We can conclude that both sources are XRBs.

XMM-23. This source is located about $2'$ south of the central bulge at a deprojected distance of about 2.4 kpc. It displays a very soft spectrum that fits well with an absorbed cool BBODY ($kT \sim 60 \text{ eV}$, $\chi^2_\nu \sim 1.3$) model with an unabsorbed luminosity of $L_X \sim 6 \times 10^{37} \text{ erg s}^{-1}$. Its short-term light curve does not show definite variability, but the long-term light curve shows variations spanning $\sim 2 \text{ yr}$. With this cool temperature, similar to those found in other galaxies (Swartz et al. 2002; Di Stefano et al. 2004), it can be classified as an SSS. These are known as cataclysmic binaries accreting at a high rate where hydrogen on the surface of the white dwarf is burned, leading to an Eddington luminosity (Di Stefano & Kong 2003).

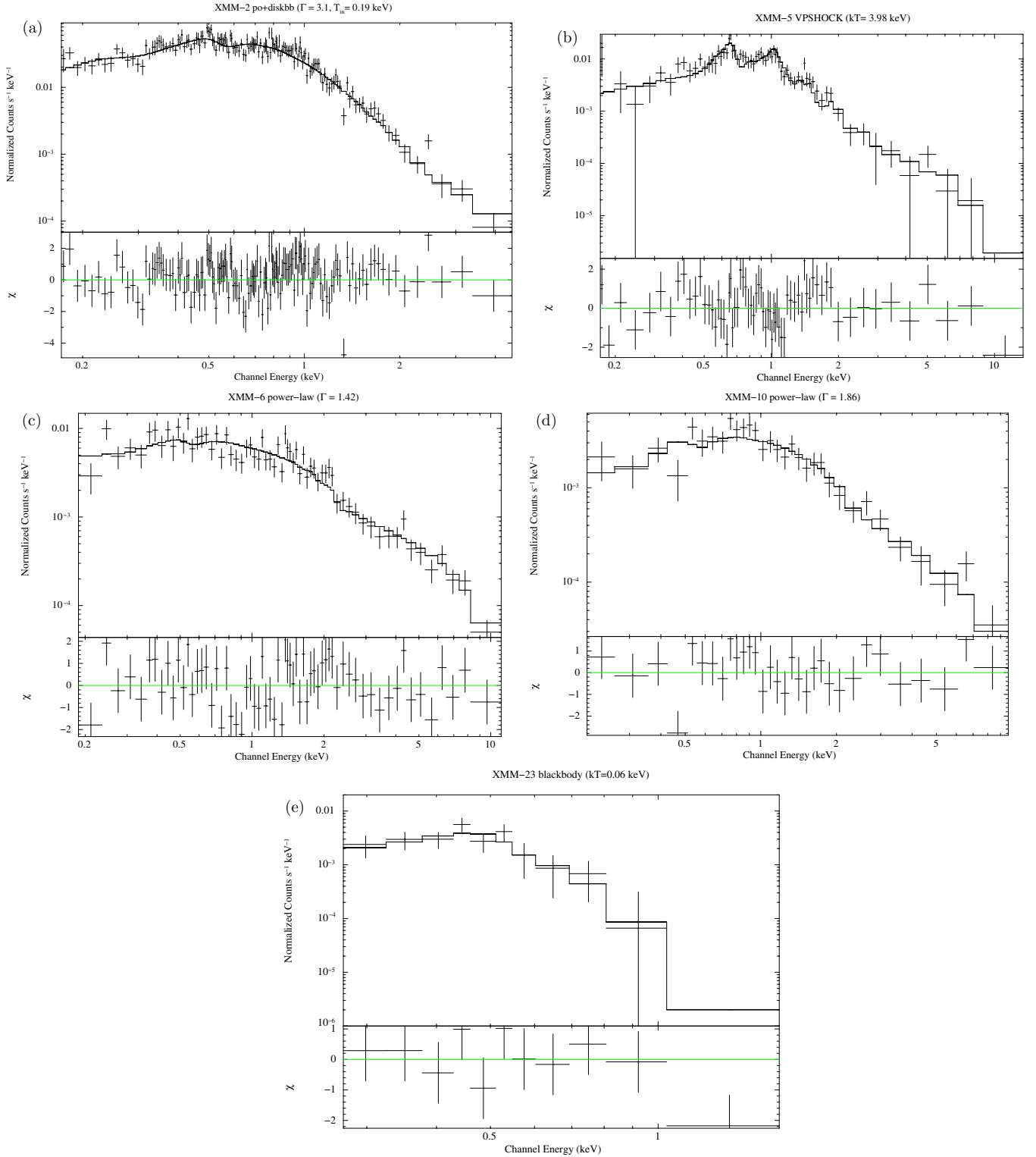


Figure 9. Best-fitting model spectra (upper panels) and the residuals between the data and the model in standard deviations (lower panels) of the sources in NGC 4395. Since the MOS data have poor statistics, only the EPIC-pn spectra have been obtained for these sources.

(A color version of this figure is available in the online journal.)

5.2. NGC 4736

We determined 21 point sources within the galaxy's D_{25} boundaries. These sources and relevant parameters are given in Table 4. The detection limiting flux in the 0.2–12 keV energy band is $\sim 2 \times 10^{-15}$ erg cm $^{-2}$ s $^{-1}$ for sources inside the optical disk. We were able to obtain X-ray spectra of four of them.

These sources have not been studied in the X-ray before. The spectral parameters for these sources including unabsorbed flux and luminosities are given in Tables 12 and 13. The fitted spectra for these sources are plotted in Figure 11. For the individual sources we note the following.

XMM-2. This source is located in the disk of the galaxy. A one-component BREMSS model fitted to data yields a good fit

Table 12
Spectral Parameters Obtained with One-component Model Fits for Point Sources in NGC 4736

Source	Model	N_H (10^{22} cm^{-2})	Γ	kT (keV)	χ^2/dof	F (10^{-13}) ($\text{erg cm}^{-2} \text{ s}^{-1}$)	L (10^{38}) (erg s^{-1})
XMM-2	PL	$0.09^{+0.009}_{-0.007}$	$2.15^{+0.04}_{-0.03}$		768.60/519	1.20	2.77
	DISKBB	<0.008		$0.87^{+0.02}_{-0.02}$	695.47/519	6.72	15.52
	BREMSS	$0.03^{+0.004}_{-0.003}$		$3.07^{+0.17}_{-0.16}$	534.87/519	8.53	19.70
XMM-12	PL	$0.04^{+0.04}_{-0.04}$	$1.47^{+0.31}_{-0.23}$		16.17/19	0.54	1.24
	DISKBB	$0.01^{+0.06}_{-0.01}$		$1.44^{+0.38}_{-0.19}$	17.09/19	0.23	0.73
	BREMSS	$0.03^{+0.04}_{-0.03}$		$12.95^{+11.43}_{-7.43}$	15.69/19	0.42	0.97
XMM-18	PL	$0.09^{+0.06}_{-0.09}$	$1.39^{+0.26}_{-0.19}$		17.42/20	0.31	0.71
	DISKBB	$0.02^{+0.05}_{-0.02}$		$1.97^{+0.55}_{-0.98}$	19.80/20	0.24	0.50
	BREMSS	$0.07^{+0.05}_{-0.07}$		$25.54^{+25.61}_{-18.02}$	17.58/20	0.29	0.66

Notes. Sources in this galaxy cannot be modeled by a BBODY model. The best-fitting model is highlighted in bold.

Table 13
Spectral Parameters Obtained with Two-component Model Fits for Point Sources in NGC 4736

Source	Model	N_H (10^{22} cm^{-2})	Γ	kT (keV)	χ^2/dof	F (10^{-13}) ($\text{erg cm}^{-2} \text{ s}^{-1}$)	L (10^{38}) (erg s^{-1})
XMM-2	PL+BBODY	$0.03^{+0.005}_{-0.006}$	$1.92^{+0.07}_{-0.06}$	$0.44^{+0.03}_{-0.03}$	576.06/517	8.97	20.72
	PL+DISKBB	$0.02^{+0.008}_{-0.006}$	$1.72^{+0.14}_{-0.13}$	$0.75^{+0.06}_{-0.04}$	530.81/517	8.44	19.49
	PL+MEKAL	$0.06^{+0.008}_{-0.009}$	$2.05^{+0.06}_{-0.06}$	$2.55^{+0.44}_{-0.35}$	718.94/517	9.92	24.51
XMM-12	PL+BBODY	$0.05^{+0.08}_{-0.05}$	$1.81^{+2.22}_{-0.86}$	$0.98^{+0.98}_{-0.98}$	15.48/17	0.54	1.23
	PL+DISKBB	$0.09^{+0.12}_{-0.08}$	$1.57^{+0.42}_{-0.32}$	$0.04^{+1.07}_{-0.04}$	15.52/17	0.67	1.40
	PL+MEKAL	$0.05^{+0.29}_{-0.05}$	$5.64^{+0.48}_{-0.22}$	10.70	15.77/17	1.14	2.63
XMM-18	PL+BBODY	$0.44^{+0.68}_{-0.39}$	$1.58^{+0.88}_{-0.49}$	$0.09^{+0.14}_{-0.03}$	14.62/18	1.24	2.59
	PL+DISKBB	$0.54^{+0.64}_{-0.44}$	$1.66^{+0.81}_{-0.54}$	$0.10^{+0.16}_{-0.01}$	14.78/18	3.29	6.87
	PL+MEKAL	$0.31^{+0.60}_{-0.12}$	$1.45^{+0.50}_{-0.34}$	$0.21^{+0.24}_{-0.06}$	13.60/18	5.30	11.07

Note. The best-fitting model is highlighted in bold.

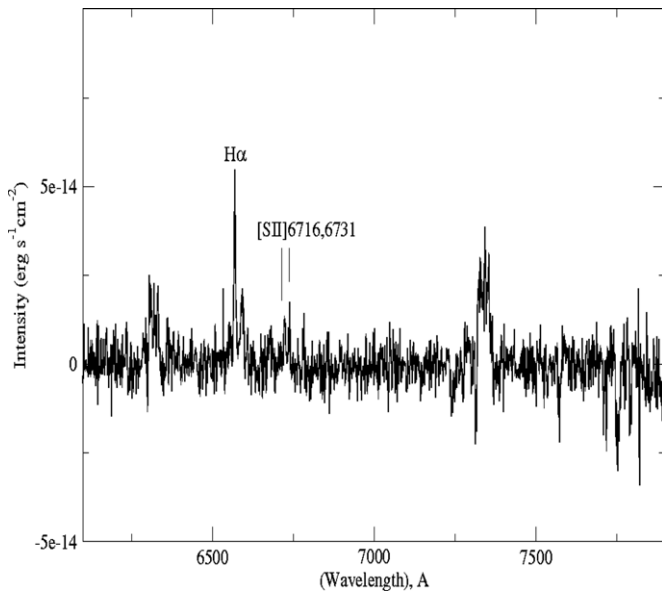


Figure 10. Optical spectrum of XMM-5 in NGC 4395 obtained with the TFOSC instrument on RTT150 at TUG, Antalya, Turkey.

with a $\chi^2_\nu \sim 1$; however, the fitted temperature ($kT = \sim 3.1$ keV) is rather high. A two-component model PL+DISKBB, on the other hand, gives a good fit with the same χ^2_ν and a lower value of $kT \sim 0.75$ keV. In the earlier work by WMR2006 using archival

data of *XMM-Newton*, this source was not detected; however, we were able to find the source about one month later in the next data set (see Table 3). Its short-term light curve (Figure 5) shows episodes of significant variability. In the long term, it has brightened by a factor of ~ 25 in the *XMM-Newton* observations during a >6 year period. It has a high unabsorbed luminosity of $L_X = 1.95 \times 10^{39} \text{ erg s}^{-1}$, revealing that this source could be a transient ULX.

XMM-12. This source is located away from the disk of the galaxy and was detected earlier by *ROSAT* (Roberts et al. 1999). In our analysis, its spectrum is adequately fitted by the one-component DISKBB model ($T_{\text{in}} = 1.44$ keV) with an unabsorbed luminosity of $L_X = 0.7 \times 10^{38} \text{ erg s}^{-1}$. Although it does not show any short-term variability, in the long term a variability within a factor of three cannot be excluded. It could be an XRB source.

XMM-18. This source was first observed by *ROSAT* (Roberts et al. 1999). It is located ~ 2.1 away from the central region of galaxy. The source spectrum is best fitted by a PL ($\Gamma = 1.39$) with an unabsorbed luminosity of $L_X = 0.7 \times 10^{38} \text{ erg s}^{-1}$. While no significant variability is found in the short term, in the long term a variability pattern of up to a factor of three is noticeable. We suggest that this source is probably an XRB.

5.3. NGC 4258

We detected 24 sources inside the D_{25} region of this galaxy (see Table 5). Our detection limiting flux is

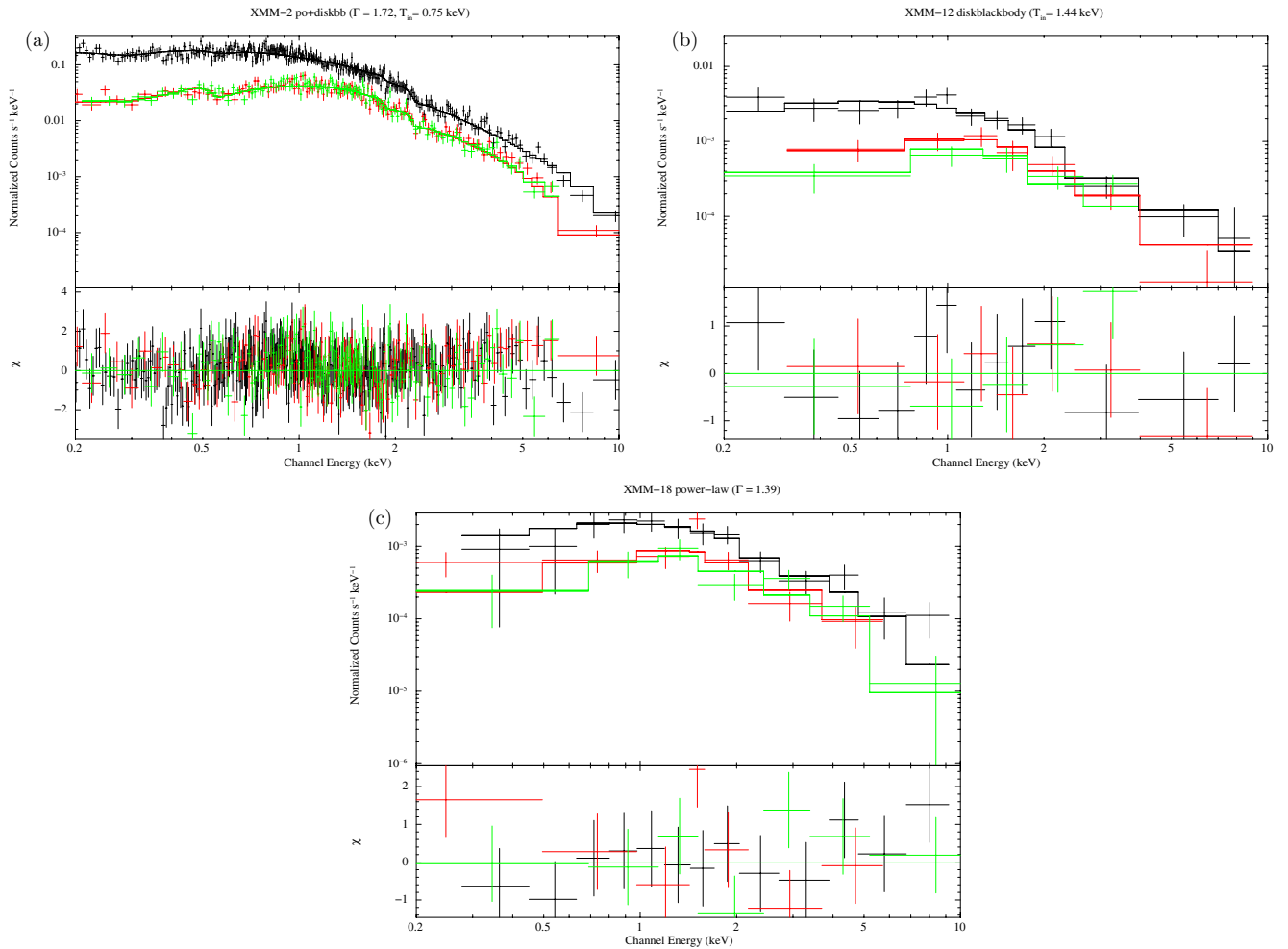


Figure 11. Best-fitting model spectra (upper panels) and the residuals between the data and the model in standard deviations (lower panels) of the sources in NGC 4736. The EPIC-pn data points and the best-fitting model are shown in black; data from MOS1 and MOS2 are shown in green and red, respectively.

(A color version of this figure is available in the online journal.)

$\sim 5 \times 10^{-15} \text{ erg cm}^{-2} \text{ s}^{-1}$ in the 0.2–12 keV energy band for sources inside the optical disk. More than half of these sources have high luminosity ($L_X > 10^{38} \text{ erg s}^{-1}$). We derived one- and two-component best-fitting spectral model parameters for the sources as given in Tables 14 and 15. The spectra of the best-fitting models for eight of these sources are given in Figure 12. Individual source characteristics are given in the following.

XMM-2. We find that this source is a transient ULX. Earlier *XMM-Newton* data had already been interpreted by WMR2006 as a transient. The source was detected for the first time in 2002 (ObsID 0059140901) and was not detected in other available observations. The sharp increase in count rates in 2002 data compared with the previous (2000, 2001) and the subsequent (2006) upper limit leads us to firmly conclude that it possesses a transient nature. The source also shows short-term variability. Its spectrum is best described by DISKBB ($T_{\text{in}} = 1.43 \text{ keV}$) with a χ^2_{ν} value of 1.33 and a high unabsorbed luminosity, $L_X = 1.5 \times 10^{39} \text{ erg s}^{-1}$. The spectral fit is not improved with an additional component. Our luminosity estimation for a one-component model is consistent with a ULX.

XMM-3. The location of this source is quite far from the disk (2'.1). This source was first detected by *ROSAT* (Pietsch et al. 1994). It was also identified as a ULX by *XMM-Newton* (WMR2006) and *Chandra* (Swartz et al. 2004). According to

WMR2006, the source is best fitted with a PL + BB model ($kT = 0.78 \text{ keV}$ and $\Gamma = 2.02$) with a χ^2_{ν} value of 1.2 for the data in 2002. This source was identified by *Chandra* as (CXOU J121857.8+471607) with an absorbed PL model ($\Gamma = 2$).

In our *XMM-Newton* analysis, the source spectrum is best fitted with a one-component absorbed DISKBB ($T_{\text{in}} = 1.28 \text{ keV}$) with a rather high unabsorbed luminosity of $L_X = 1.9 \times 10^{39} \text{ erg s}^{-1}$. Our analysis of the *Chandra* data for this source also shows that its spectrum is best fitted with a hot DISKBB model, ($T_{\text{in}} = 1.31 \text{ keV}$) with a higher unabsorbed luminosity of $L_X = 2.8 \times 10^{39} \text{ erg s}^{-1}$. Its short-term light curve shows a significant variation; its long-term light curve also shows variation with a factor of ~ 4 . The high source luminosity leads us to conclude that it is a ULX. We also note that the present analysis is based on a longer observation time with much better statistics than all earlier results.

XMM-6. This source is located 2'.4 away from the galactic center. Its spectrum is well fitted with an absorbed PL ($\Gamma = 1.87$) model. It has an unabsorbed luminosity of $L_X = 1.5 \times 10^{39} \text{ erg s}^{-1}$. A single-component model fitted to the *Chandra* data gives almost the same parameter ($\Gamma = 1.87$), and a similarly high luminosity $\sim 1 \times 10^{39} \text{ erg s}^{-1}$, helping us to identify the source as a ULX (Swartz et al. 2004). Our *Chandra* data analysis for this source also gives the same best-fitted model (PL) and a parameter with almost the same high-luminosity value.

Table 14
Spectral Parameters Obtained with One-component Model Fits for Point Sources in NGC 4258

Source	Model	N_{H} (10^{22} cm^{-2})	Γ	kT (keV)	χ^2/dof	F (10^{-13}) ($\text{erg cm}^{-2} \text{ s}^{-1}$)	L (10^{38}) (erg s^{-1})
XMM-2*	PL	$0.18^{+0.07}_{-0.06}$	$1.90^{+0.21}_{-0.22}$		31.80/22	3.96	23.87
	DISKBB	$0.02^{+0.03}_{-0.02}$		$1.43^{+0.30}_{-0.25}$	29.28/22	2.53	15.25
	BREMSS	$0.11^{+0.04}_{-0.04}$		$5.50^{+2.86}_{-1.74}$	29.91/22	3.14	18.96
XMM-3	PL	$0.56^{+0.07}_{-0.06}$	$2.19^{+0.07}_{-0.07}$		297/231	6.60	39.77
	DISKBB	$0.27^{+0.05}_{-0.03}$		$1.28^{+0.05}_{-0.05}$	221.14/231	3.23	19.46
	BREMSS	$0.41^{+0.05}_{-0.04}$		$3.91^{+0.30}_{-0.39}$	237.76/231	4.23	25.49
XMM-6	PL	$0.21^{+0.03}_{-0.03}$	$1.87^{+0.09}_{-0.09}$		136.61/142	2.57	15.48
	DISKBB	$0.06^{+0.01}_{-0.01}$		$1.39^{+0.10}_{-0.09}$	161.22/142	1.63	9.82
	BREMSS	$0.15^{+0.02}_{-0.02}$		$5.60^{+1.17}_{-0.84}$	135.84/142	2.03	12.23
XMM-8	PL	$0.12^{+0.02}_{-0.02}$	$2.19^{+0.14}_{-0.12}$		125.29/109	2.04	12.28
	DISKBB	0.01		0.83	249.70/109	1.01	6.08
	BREMSS	$0.05^{+0.01}_{-0.01}$		$3.20^{+0.56}_{-0.47}$	166.01/109	1.37	8.25
XMM-10	PL	$0.58^{+0.05}_{-0.05}$	$2.80^{+0.15}_{-0.14}$		87.67/96	1.54	9.28
	DISKBB	$0.27^{+0.10}_{-0.10}$		$0.84^{+0.10}_{-0.09}$	87.16/96	1.83	11.02
	BREMSS	$0.39^{+0.04}_{-0.03}$		$2.00^{+0.26}_{-0.23}$	86.82/96	2.61	15.73
XMM-16	PL	$0.27^{+0.04}_{-0.04}$	$2.20^{+0.18}_{-0.15}$		99.78/76	1.20	7.23
	DISKBB	$0.07^{+0.02}_{-0.02}$		$0.85^{+0.10}_{-0.10}$	146.78/76	0.68	4.10
	BREMSS	$0.14^{+0.03}_{-0.02}$		$2.59^{+0.53}_{-0.45}$	117.96/76	0.94	5.72
XMM-17	PL	$0.15^{+0.03}_{-0.03}$	$1.99^{+0.12}_{-0.10}$		117.13/80	0.95	3.31
	DISKBB	0.05		1.10	169.73/80	0.55	3.31
	BREMSS	$0.09^{+0.02}_{-0.01}$		$4.32^{+1.09}_{-0.88}$	131.37/80	0.72	4.34
XMM-21	PL	$0.08^{+0.03}_{-0.03}$	$1.99^{+0.11}_{-0.09}$		85.67/78	0.34	2.05
	DISKBB	0.00		$0.93^{+0.10}_{-0.10}$	100.56/78	0.20	1.20
	BREMSS	$0.02^{+0.02}_{-0.01}$		$4.07^{+1.15}_{-0.89}$	81.61/78	0.29	1.74

Notes. Sources in this galaxy cannot be modeled by a BBODY model and the best-fitting model for each source is highlighted in bold.

* The spectra of this source were obtained by using only the EPIC-pn data.

The long-term light curve of XMM-6 shows a factor of ~ 3 variability between the intervals, and there is also strong evidence for short-term variability. This raises the possibility that it could be an accreting XRB in the galaxy. Interestingly, however, the same source also coincides with a blue stellar counterpart from the DSS2 image, making it a likely background AGN candidate. The true nature of this source requires further study.

XMM-8. This source is best described by a two-component model. The spectral fit is improved over that of a simple PL ($\Gamma = 2.1$) fit by the addition of a MEKAL component ($\Gamma = 1.95$ and $kT = 0.57 \text{ keV}$). It has a high unabsorbed luminosity of $L_X = 1.2 \times 10^{39} \text{ erg s}^{-1}$. To reveal its nature we also analyzed the *Chandra* archival data. Two different sources can be resolved within the same position by the better angular resolution of *Chandra*. However, due to the limited amount of data, it was not possible for us to carry out a satisfactory spectral analysis for these two separate sources. In the same neighborhood, two radio SNR candidates were identified by Hyman et al. (2001; sources 10 and 12, Table 1) but none coincide with our *Chandra* sources (angular separations $\sim 6''$ and $\sim 16''$, respectively). Both long-term and short-term light curves of the data from the source region do show evidence of sometimes erratic variability. The spectral shape discussed above leads us to tentatively conclude

that the source region could harbor an XRB. However, further long-duration observations with better angular resolution are certainly needed to clarify the nature of the source(s).

XMM-10. This source is located far away ($6.4'$) from the central body of the galaxy. Its spectrum is best fitted with an absorbed PL model ($\Gamma = 2.8$, $\chi^2_\nu = 0.9$). The unabsorbed luminosity in this observation is $L_X = 9.2 \times 10^{38} \text{ erg s}^{-1}$. Its short-term light curve shows no strong indication of variability. However, its long-term light curve does show variability (an uninterrupted increase) by a factor of at least five over the time interval of a decade. This source could be an XRB.

XMM-16. This source gives a best spectral fit with a PL model ($\Gamma = 2.20$). The unabsorbed X-ray luminosity is $L_X = 7.2 \times 10^{38} \text{ erg s}^{-1}$. The short-term light curve shows significant variability and the long-term data show evidence of variability within a factor of ~ 4 after 2002 over the next ~ 4 years. The spectral parameters and variation of the source suggest that this could also be a candidate XRB.

XMM-17. This source is located $\sim 2'$ away from the main body of the galaxy and its spectrum is described by a PL with $\Gamma \sim 2$ with an unabsorbed luminosity of $L_X = 3.3 \times 10^{38} \text{ erg s}^{-1}$. Its short-term light curve shows a significant level of variability, while its long-term data show a factor of ~ 3 variation between observations. This source may also be a candidate XRB.

Table 15
Spectral Parameters Obtained with Two-component Model Fits for Point Sources in NGC 4258

Source	Model	N_H (10^{22} cm^{-2})	Γ	kT (keV)	χ^2/dof	F (10^{-13}) ($\text{erg cm}^{-2} \text{ s}^{-1}$)	L (10^{38}) (erg s^{-1})
XMM-2*	PL+BBODY	$0.16^{+0.14}_{-0.15}$	$2.24^{+0.27}_{-0.72}$	$0.88^{+0.55}_{-0.40}$	27.76/20	4.05	24.42
	PL+DISKBB	$0.11^{+0.34}_{-0.05}$	$2.12^{+1.59}_{-1.59}$	$1.40^{+1.12}_{-0.47}$	27.35/20	2.80	16.88
	PL+MEKAL	$0.10^{+0.05}_{-0.04}$	$9.45^{+9.89}_{-9.89}$	$4.25^{+1.44}_{-0.89}$	37.11/20	7.89	47.57
XMM-3	PL+BBODY	$0.37^{+0.10}_{-0.09}$	$2.16^{+0.10}_{-0.22}$	$0.76^{+0.08}_{-0.07}$	244.56/229	4.39	19.76
	PL+DISKBB	$0.28^{+0.02}_{-0.02}$	$0.67^{+19.67}_{-9.67}$	$1.23^{+0.06}_{-0.06}$	219.18/229	3.28	19.76
	PL+MEKAL	$0.75^{+0.17}_{-0.08}$	$2.37^{+0.13}_{-0.07}$	$0.14^{+0.08}_{-0.02}$	278.16/229	4.82	29.05
XMM-6	PL+BBODY	$0.21^{+0.05}_{-0.03}$	$1.97^{+0.24}_{-0.16}$	$0.94^{+0.64}_{-0.37}$	133.26/140	2.30	13.85
	PL+DISKBB	$0.23^{+0.26}_{-0.08}$	$2.27^{+2.26}_{-0.68}$	$2.04^{+2.66}_{-1.38}$	133.54/140	2.42	14.58
	PL+MEKAL	$0.19^{+0.19}_{-0.02}$	$1.80^{+0.21}_{-0.12}$	4.12	135.64/140	2.22	13.37
XMM-8	PL+BBODY	$0.28^{+0.09}_{-0.04}$	$3.57^{+0.30}_{-0.46}$	$1.44^{+0.35}_{-0.26}$	94.53/107	7.84	47.24
	PL+DISKBB	$0.12^{+0.02}_{-0.02}$	$2.19^{+0.14}_{-0.12}$	0.00	124.87/107	2.86	17.23
	PL+MEKAL	$0.09^{+0.02}_{-0.01}$	$1.95^{+0.07}_{-0.13}$	$0.57^{+0.05}_{-0.04}$	105.93/107	1.96	11.81
XMM-10	PL+BBODY	$0.58^{+0.06}_{-0.05}$	$2.79^{+0.17}_{-0.14}$	199.36	81.24/92	5.19	31.27
	PL+DISKBB	$0.56^{+0.23}_{-0.24}$	$3.05^{+2.00}_{-1.02}$	$0.99^{+0.46}_{-0.41}$	77.65/92	5.13	30.91
	PL+MEKAL	$0.58^{+0.08}_{-0.08}$	$2.94^{+0.25}_{-0.29}$	$2.95^{+0.42}_{-0.51}$	79.81/92	1.85	11.14
XMM-16	PL+BBODY	$0.29^{+0.05}_{-0.05}$	$2.61^{+0.24}_{-0.35}$	199.36	99.31/74	2.16	13.02
	PL+DISKBB	$0.27^{+0.32}_{-0.08}$	$2.47^{+0.08}_{-0.08}$	$0.98^{+0.03}_{-0.05}$	101.47/74	1.6	9.64
	PL+MEKAL	$0.17^{+0.04}_{-0.04}$	$2.09^{+0.10}_{-0.14}$	$0.65^{+0.19}_{-0.22}$	76.69/74	0.43	2.59
XMM-17	PL+BB	$0.20^{+0.17}_{-0.05}$	$1.69^{+0.33}_{-0.18}$	$0.14^{+0.03}_{-0.04}$	101.54/78	1.12	6.75
	PL+DISKBB	$0.30^{+0.14}_{-0.08}$	$1.74^{+0.19}_{-0.24}$	$0.16^{+0.05}_{-0.04}$	101.55/78	1.83	11.03
	PL+MEKAL	$0.07^{+0.04}_{-0.03}$	$1.68^{+0.17}_{-0.14}$	$3.32^{+0.12}_{-0.09}$	76.36/78	0.42	2.53
XMM-21	PL+BB	$0.10^{+0.05}_{-0.08}$	$2.21^{+1.03}_{-0.16}$	$0.97^{+0.12}_{-0.09}$	84.56/76	0.34	2.05
	PL+DISKBB	$0.13^{+0.05}_{-0.04}$	$2.12^{+0.21}_{-0.19}$	$0.02^{+0.01}_{-0.01}$	80.06/76	0.32	1.92
	PL+MEKAL	$0.06^{+0.05}_{-0.04}$	$1.91^{+0.24}_{-0.26}$	$2.90^{+2.91}_{-2.91}$	94.63/76	0.33	1.98

Note. * The spectra of this source were obtained by using only the EPIC-pn data.

XMM-21. In our analysis, this source was best fitted with a one-component absorbed PL model ($\Gamma \sim 2$). Both its short-term and long-term data show strong evidence for variability. The source has an unabsorbed luminosity of $L_X = 2.0 \times 10^{38} \text{ erg s}^{-1}$, which suggests that this source is likely to be an XRB. However, in the [WMR2006](#) list it was defined as a ULX. Its spectrum was fitted with a PL and a BREMSS equally well at a luminosity $L_X = 1.2 \times 10^{39} \text{ erg s}^{-1}$. Therefore, further observations are needed to clarify its true nature.

6. DISCUSSION AND CONCLUSIONS

In the above sections, we presented spectral and temporal analyses of the non-nuclear X-ray point sources in three nearby galaxies, NGC 4395, NGC 4736, and NGC 4258, selected on the basis of their low hydrogen column densities with low activity Seyfert nuclei. Our main conclusions can be noted as follows.

1. The total number of point sources in the D_{25} area of each of these galaxies is similar (29 for NGC 4395, 21 for NGC 4736, and 23 for NGC 4258). Data at hand, however, allow spectral analysis for only a smaller number (a total of 16 out of 74) of these sources. The luminosity of these sources falls into the range $(0.4\text{--}22.7) \times 10^{38} \text{ erg s}^{-1}$. Of these 16 sources, 14 have positions clearly indicating that

they have no contamination from background or foreground objects or structures.

2. For comparison purposes, we have analyzed archival *Chandra* data of the three galaxies. Of these 16 *XMM-Newton* sources, 13 have also been detected by *Chandra*. Their source positions, in general, show a clear offset $\sim 2''$ from the center of the *XMM-Newton* error circle ($15''$). Only 2 of these 13 sources have been examined spectrally due to sufficient statistics provide by *Chandra* observations.
3. Of these 16 sources, 4 are ULX candidates owing to their spectral characteristics and high luminosities. Two of these sources are in NGC 4258 (XMM-2 and XMM-3) and they are best fitted with an absorbed DISKBB model with a hot inner disk temperature ($T_{\text{in}} \sim 1.43 \text{ keV}$ and 1.28 keV , respectively). These values are within the range given for Galactic black hole XRBs in high-state emission (McClintock & Remillard 2006). On the other hand, two ULXs (XMM-2 in NGC 4736 and XMM-2 in NGC 4258) show significant transient behavior. The statistically significant improvement over a one-component fit is found in the PL+DISKBB model fit for the ULX in NGC 4736. The disk temperature is also cool (0.75 keV) in this case. Similar disk temperatures for ULX sources in M101 (Jenkins et al. 2004) and in the interacting pair galaxies NGC 4485/4490 (Gladstone & Roberts, 2009) were already found. Based on the argument that black hole masses scale inversely with

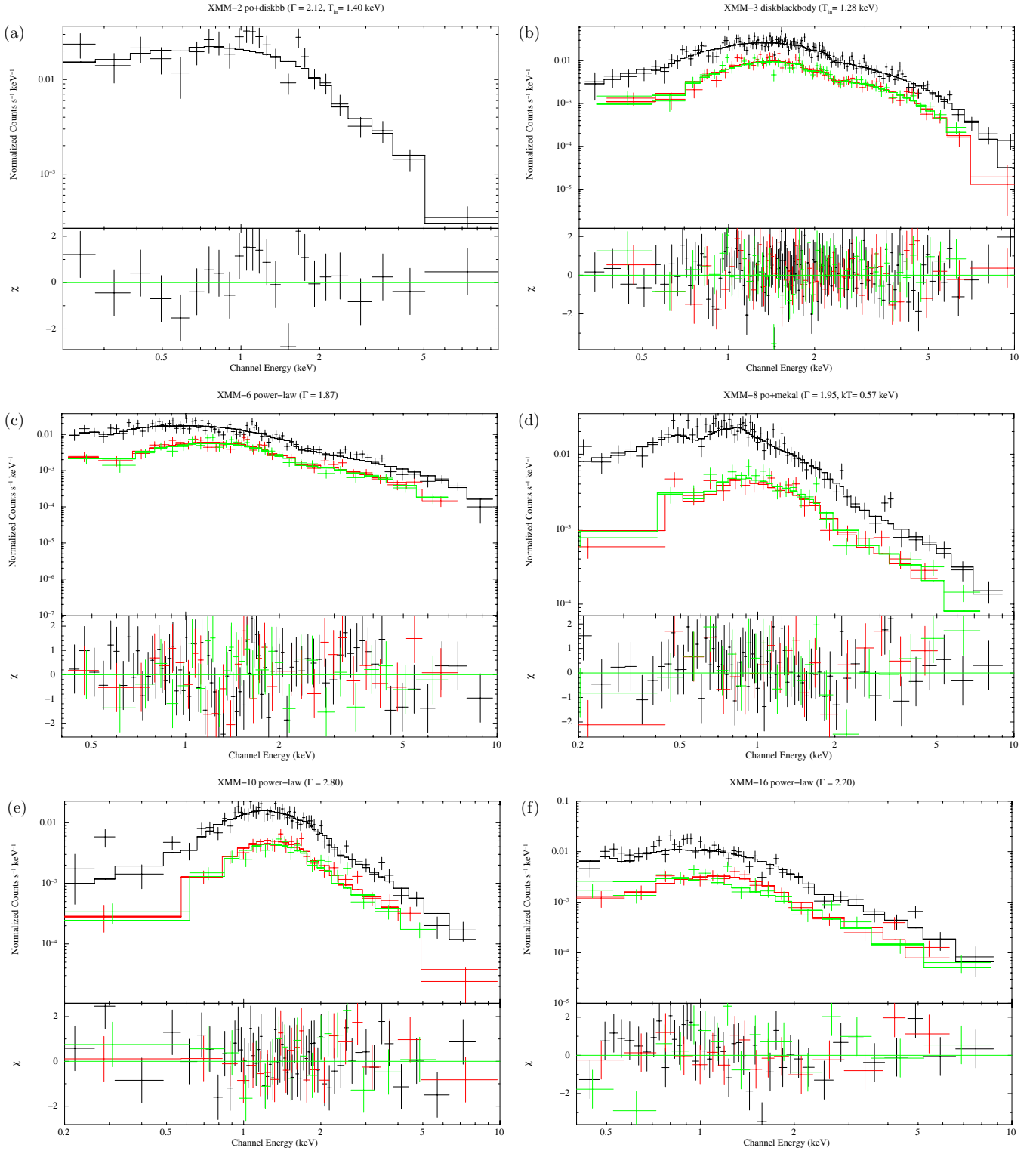


Figure 12. Best-fitting model spectra (upper panels) and the residuals between the data and the model in standard deviations (lower panels) of the sources in NGC 4258. The EPIC-pn data points and the best-fitting model are shown in black; data from MOS1 and MOS2 are shown in green and red, respectively.

(A color version of this figure is available in the online journal.)

accretion disk temperatures ($T_{\text{in}} \sim M^{-1/4}$), this was interpreted as evidence of intermediate-mass black holes with masses in the range of 10^2 – $10^4 M_{\odot}$ for some ULX sources (Colbert & Mushotzky 1999). On the other hand, assuming spherical accretion onto a central black hole in a binary system at the Eddington limit as suggested by Makishima

et al. (2000), our point source luminosities imply black hole masses in the stellar range of $(2\text{--}15) M_{\odot}$. This is consistent with Galactic stellar-mass black holes, which were found to lie in the range of $(2\text{--}23) M_{\odot}$ (McClintock & Remillard 2006). Most probably, these sources belong to the extreme end of the XRB population in their galaxies. Many similar

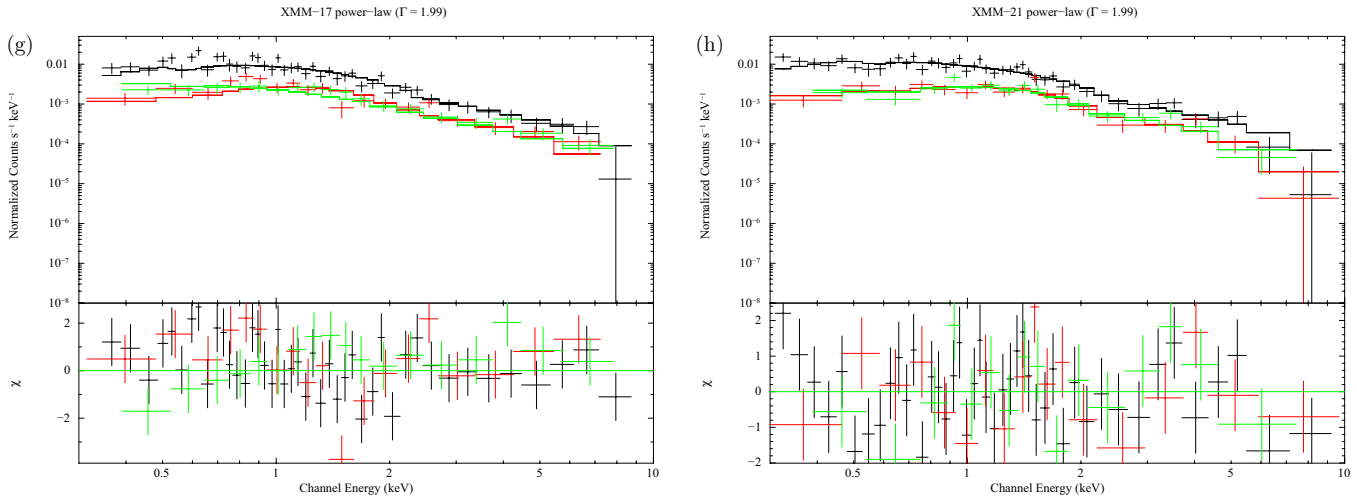


Figure 12. (Continued)

luminous point sources in nearby galaxies are also reported (Jenkins et al. 2004; Gladstone & Roberts 2009).

4. Of the remaining 12 sources, 8 are best fitted with absorbed PL spectra ($\Gamma = 1.4\text{--}2.8$). They generally have luminosities around the Eddington limit ($\geq 10^{38}$). Photon indices of seven of these sources are in agreement with low/hard-state black hole XRBs (Tanaka 2001). The remaining two sources (XMM-10 and XMM-16 in NGC 4258) have steeper power-law slopes ($\Gamma > 2$), representing strong Comptonized thermal emission from a black hole accretion disk (Jenkins et al. 2004; McClintock & Remillard 2006). Based on X-ray data these sources are considered to be black hole XRBs.
5. The locations of the point sources could also provide clues to the nature of the X-ray emission; however, at times they could also be misleading. The positions of our sources suggest that almost all are associated with their host galaxies except possibly one. As explained above, this source (XMM-6 in NGC 4258) could be a background AGN due to its spectral shape (PL with $\Gamma \sim 1.9$, which is typical of AGNs) and its coincidence with a stellar object (in the corresponding DSS image), warranting further investigation.
6. A noticeable overall result of the spectral analysis of the sources from these three galaxies is that X-ray sources from different classes can be distinguished. One source (XMM-5 of NGC 4395) is distinctly different from the rest. A closer inspection by our optical follow-up observation revealed that it was indeed a different type—an SNR with a best spectral fit to a VPSHOCK, which is typical of such objects (Sonbas et al. 2010).
7. We have identified only one SSS with typical low-luminosity values around $5 \times 10^{37} \text{ erg s}^{-1}$ in one of these galaxies (XMM-23 in NGC 4395). This class of source is generally known to be a white dwarf accreting at high rates, resulting in nuclear burning on the surface with $kT \sim (10\text{--}100) \text{ eV}$ (Di Stefano et al. 2004; Stiele et al. 2010). Our source also confirms these limits.
8. About half of the sources analyzed here show statistically significant short- and long-term variabilities. This can be taken as evidence for the underlying binary nature of these sources.

In more general terms, we can conclude that X-ray astronomy has reached a stage where it is possible to differentiate several source types in the galaxies beyond our local group. With increasing statistics, the role of such sources in the evolution of stars and such galaxies will become clearer.

Aysun Akyuz acknowledges support from the EU FP6 Transfer of Knowledge Project “Astrophysics of Neutron Stars” (MKTD-CT-2006-042722). We thank Frank Haberl and Nazim Aksaker for their very valuable help. We also thank the TUBITAK National Observatory (TUG) for support with observing times and equipment.

REFERENCES

- Borkowski, J. K., Szymkowiak, A. E., Blondin, J. M., & Sarazin, C. L. 1996, *ApJ*, **466**, 866
- Cecil, G., Morse, J. A., & Veilleux, S. 1995, *ApJ*, **452**, 613
- Cedres, B., & Cepa, J. 2002, *A&A*, **391**, 809
- Colbert, E. J. M., & Mushotzky, R. F. 1999, *ApJ*, **519**, 89
- Courtes, G., Petit, H., Hua, C. T., et al. 1993, *A&A*, **268**, 419
- Cui, W., Feldkhun, D., & Braun, R. 1997, *ApJ*, **477**, 693
- Dickey, J. M., & Lockman, F. J. 1990, *ARA&A*, **28**, 215
- Di Stefano, R., & Kong, A. K. H. 2003, *ApJ*, **592**, 884
- Di Stefano, R., Kong, A. K. H., Greiner, J., et al. 2004, *ApJ*, **610**, 247
- Eracleous, M., Shields, J. C., Chartas, G., & Moran, E. C. 2002, *ApJ*, **565**, 108
- Fabbiano, G. 1989, *A&A*, **27**, 87
- Filippenko, A. V., & Sargent, W. L. W. 1985, *ApJS*, **57**, 503
- Filippenko, A. V., & Sargent, W. L. W. 1989, *ApJ*, **347**, 11
- Gabriel, C., et al. 2004, in ASP Conf. Ser. 314, *Astronomical Data Analysis Software and Systems (ADASS) XIII*, ed. F. Ochsenbein, M. G. Allen, & D. Egret (San Francisco, CA: ASP), 759
- Gladstone, T. C., & Roberts, T. P. 2009, *MNRAS*, **397**, 124
- Hyman, S. D., Calle, D., Weiler, K. W., et al. 2001, *ApJ*, **551**, 702
- Jansen, F., Lumb, D., Altieri, B., et al. 2001, *A&A*, **365**, L1
- Jenkins, L. P., Roberts, T. P., Warwick, R. S., Kilgard, R. E., & Ward, M. J. 2004, *MNRAS*, **349**, 404
- Kong, A. K. H., Garcia, M. R., Primi, F. A., et al. 2002, *ApJ*, **557**, 738
- Kong, A. K. H., Sjouwerman, L. O., Williams, B. F., Garcia, M. R., & Dickel, J. R. 2003, *ApJL*, **590**, L21
- Leonidaki, I., Zezas, A., & Boumis, P. 2010, *ApJ*, **725**, 842
- Lira, P., Lawrence, A., O’Brien, P., et al. 1999, *MNRAS*, **305**, 109
- Liu, J. 2011, *ApJS*, **192**, 10
- Makishima, K., Fujimoto, R., Ishisaki, Y., et al. 1994, *PASJ*, **46**, L77
- Makishima, K., Kubota, A., Mizuno, T., et al. 2000, *ApJ*, **535**, 632
- Mathewson, D. S., & Clarke, J. N. 1973, *ApJ*, **182**, 697
- McClintock, J. E., & Remillard, R. A. 2006, in *Compact Stellar X-ray Sources*, ed. W. H. G. Lewin & van der Klis (Cambridge: Cambridge Univ. Press)

- Miyoshi, M., James, M., James, H., et al. 1995, *Natur*, 377, 177M
- Moran, E. C., Eracleous, M., Leighly, K. M., et al. 2005, *AJ*, 129, 2108
- Moran, E. C., Filippenko, A. V., Ho, L. C., et al. 1999, *PASP*, 111, 801
- Pellegrini, P. S., Fabbiano, G., Fiore, F., Trinchieri, G., & Antonelli, A. 2002, *A&A*, 383, 1
- Pence, W. D., Snowden, S. L., Mukai, K., & Kuntz, K. D. 2001, *ApJ*, 561, 189
- Pietsch, W. 2004, *A&A*, 426, 11
- Pietsch, W. 2005, *A&A*, 434, 483
- Pietsch, W., & Read, A. M. 2002, *A&A*, 384, 793
- Pietsch, W., Vogler, A., Kahabka, P., Jain, A., & Klein, U. 1994, *A&A*, 284, 386
- Plucinsky, P. P., Williams, B., Long, K. S., et al. 2008, *ApJS*, 174, 366
- Roberts, T. P., Warwick, R. S., & Ohashi, T. 1999, *MNRAS*, 304, 52
- Sonbas, E., Akyüz, A., Balman, Ş., & Özel, M. E. 2010, *A&A*, 517, A91
- Stiele, H., et al. 2010, *AN*, 999, 789
- Stobart, M. A., Robert, T. P., & Wilms, J. 2006, *MNRAS*, 368, 397
- Strüder, R., Aschenbach, B., Bruninger, H., et al. 2001, *A&A*, 375, L5
- Swartz, D. A., Ghosh, K. K., McCollough, M. L., et al. 2003, *ApJS*, 144, 213
- Swartz, D. A., Ghosh, K. K., Suleimanov, V., Tennant, A. F., & Wu, K. 2002, *ApJ*, 574, 382
- Swartz, D. A., Ghosh, K. K., Tennant, A. F., & Wu, K. 2004, *ApJ*, 154, 519
- Tanaka, Y. 2001, in *Black Holes in Binaries and Galactic Nuclei*, ed. L. Kaper, E. P. J. van den Heuvel, & P. A. Woudt (Berlin: Springer), 141
- Turner, L. J. M., Abbey, A., Arnaud, M., et al. 2001, *A&A*, 365, L27
- Vaughan, S., Iwasawa, K., Fabian, A. C., & Hayashida, K. 2005, *MNRAS*, 356, 524
- Vogler, A., & Pietsch, W. 1999, *A&A*, 352, 64
- Winter, L. M., Mushotzky, R. F., & Reynolds, C. 2006, *ApJ*, 649, 730
- Yang, Y., Li, B., Wilson, A. S., & Reynolds, C. S. 2007, *ApJ*, 660, 1106
- Young, A. J., & Wilson, A. S. 2004, *ApJ*, 601, 133